学位論文

Measurement of the Diffractive Cross Section in Low Q^2 ep Scattering at HERA

HERAにおける低いQ^2電子陽子散乱での
回折的断面積の測定

平成10年12月博士（理学）申請

東京大学大学院理学系研究科

物理学専攻

大塚孝慈

Measurement of the Diffractive Cross Section in Low Q^2 ep Scattering at HERA

Masahide Inuzuka

University of Tokyo

7-3-1, Hongo, Bunkyo-ku, Tokyo, 133, Japan

January, 1999

Abstract

The cross section of the diffractive process, $\gamma^* + p \rightarrow X + N$, has been measured in the mass range, $3 < M_X < 12.2\,\mathrm{GeV}$ and $M_N < 6\,\mathrm{GeV}$, for the low Q^2 region, $0.220 < Q^2 < 0.700\,\mathrm{GeV}^2$, and the $\gamma^* p$ center-of-mass energy, $90 < W < 220\,\mathrm{GeV}$ using the ZEUS detector.

The Pomeron trajectory, $\alpha_{I\!P}(t)$ at $t = 0$, is obtained from the W dependence of the cross section, $d\sigma^{diff}_{\gamma^* p}/dM_X$, using the Regge formalism. The extracted value, $\alpha_{I\!P}(0) = 1.217 \pm 0.026(stat)^{+0.042}_{-0.088}(syst)$, is significantly higher than that expected from soft Pomeron.

Contents

1. Introduction

At present, quarks and leptons are considered to be the elementary particles constituting all material in our universe[1, 2]. In 1911, Rutherford detected α particles scattered from a gold target to investigate the structure of atoms[3]. On the analogy of his experiment, indirect evidence for the existence of quarks can be obtained by lepton-nucleon scattering experiments[4]. In the late 1960s, Deep Inelastic Scattering (DIS) experiments using an electron beam and a hydrogen target were carried out at SLAC to study the structure of the proton. The proton is probed by the virtual photon exchanged between the electron and the proton[5]. The resolving power is characterized by a kinematic variable Q^2, which is defined as the negative four momentum squared of the virtual photon. As Q^2 increases ($Q^2 > 1\,\mathrm{GeV}^2$), the resolution becomes fine enough to see the constituents of the proton. The data indicated that the proton has a structure and it is composed of pointlike constituents. Up to the 1980s, muon beams and neutrino beams also became available. The results of these experiments were consistent with the prediction of the Quantum Chromo Dynamics (QCD), which is thought to be the right theory for the strong interaction.

In 1992, these fixed target experiments were followed by the *ep* collider experiment at HERA (Hadron Elektron Ring Anlage). The high center-of-mass energy enables us to investigate the structure of the proton over a wider kinematic range.

In the view that the DIS is the scattering of the electron and a quark in the proton, a colour flow between the struck quark and the remnant partons produces many hadrons in the longitudinal phase space between them. However, soon after the HERA experiments started, a different type of hadronic final states was observed. In these events, only the scattered electron and particles in the direction of the struck quark were detected. The rests of particles were thought to escape into the beam pipe in the incoming proton direction. The events showed, therefore, a gap in the longitudinal phase space between two groups of the low mass hadronic systems. It was a surprise that as much as 10% of the DIS events presented such hadronic final states even at high $Q^2 (> 10\,\mathrm{GeV}^2)$. Those events were named Large Rapidity Gap (LRG) events[6, 7].

The LRG events are considered to be produced from the diffractive processes in the high energy virtual photon-proton scattering. The diffractive process is well known in the hadron interactions as discussed below.

Analytic behaviour of the high energy hadron-hadron collision is described by the Regge theory without knowing the details of the nature of interactions[8]. At high energy, the differential cross section of the elastic scattering, $A + B \to A + B$, is expected as $d\sigma/dt \propto s^{2(\alpha(t)-1)}$ where s and t are the Mandelstam variables[9], center-of-mass energy squared and four momentum transfer squared, respectively. The $\alpha(t)$ represents the Regge trajectory which is formed from particles exchanged between A and B. From the optical theorem[1], the total cross section of the process, $A + B \to X$, can be obtained as $\sigma \propto s^{\alpha(0)-1}$.

The total proton-(anti)proton cross sections were measured with various incident energies[10]. It was turned out that the cross sections are almost constant at high energy. Since the contribution of all known mesons to be exchanged gives a rapid decrease of the cross section, it is necessary to introduce the additional trajectory of $\alpha_{I\!P}(0) \sim 1$. This is referred to as the Pomeron trajectory. The Pomeron can be regarded as a virtual particle which is exchanged in the diffractive scattering.

The data of various kinds of hadron-hadron scattering are now available[11]. After introducing the Pomeron trajectory, A.Donnachie and P.V.Landshoff demonstrated that the s dependence of the total cross sections in high energy hadron-hadron collisions are described promisingly by the Regge theory with $\alpha_{I\!P}(0) = 1.0808$[12]. It is referred to as 'soft Pomeron'.

Since it is possible to explore the mass range of the virtual photon-proton system up to $\sim$200GeV where the Pomeron trajectory is dominated, it is an advantage to study the diffractive physics at HERA. Moreover, it is possible to select the Q^2 range if the scattered electron is tagged in the detector.

In photoproduction ($Q^2 = 0$), the total cross section at HERA[13, 14] turned out to be compatible with the extrapolation from the lower energy experiments, assuming the s dependence with $\alpha_{I\!P}(0) = 1.0808$. In addition, the consistent results have been obtained from the mass distribution of the photoproduction diffractive events[15, 16].

In DIS, a steeper s dependence is predicted from the QCD calculation[17, 18, 19], in which the diffractive scattering could be mediated by two-gluon exchange. In the Regge picture, it can be interpreted as the scattering mediated by the Pomeron with the higher value of $\alpha_{I\!P}(0)$. It is referred to as 'hard Pomeron'. The behaviour of the proton structure function at HERA is described successfully using the QCD. The measured structure functions can be translated into the total virtual photon-proton cross sections at $Q^2 > 1\,\mathrm{GeV}^2$[20]. The s dependence of the cross section is so steep

that it cannot be described by the soft Pomeron. Furthermore, such a steep s dependence is also observed in the exclusive vector meson productions[21, 22] and the inclusive diffractive cross sections[23, 24].

It is, therefore, important to know the s dependence of the total and diffractive cross sections as a function of Q^2. In order to investigate the Q^2 transition region between photoproduction and DIS, the Beam Pipe Calorimeter (BPC) has been installed in the ZEUS detector since 1994[25]. The $\alpha_{I\!P}(0)$ obtained from the total cross section in the low Q^2 region ($0.11 < Q^2 < 0.65\,\mathrm{GeV}^2$) turned out to be closer to the result from DIS[26, 20].

This thesis reports the measurement of the cross section of the diffractive process, $\gamma^* + p \to X + N$, in the low Q^2 region using the ZEUS 1996 data. The $\alpha_{I\!P}(0)$ in that region is extracted from the s dependence of the cross section, $d\sigma^{diff}_{\gamma^* p}/dM_X$, where M_X denotes the mass of the dissociated photon system. From the Q^2 dependence of $\alpha_{I\!P}(0)$ and the comparison with the result from the total cross section, we examine the consistency of the Regge phenomenology in the Q^2 transition region.

This thesis is organized as follows. The relevant kinematic variables are defined and the theoretical background is reviewed in the next chapter. Chapter 3 describes the experimental setup: the HERA accelerator and the ZEUS detector. The algorithm of Monte Carlo simulation is written in Chapter 4. The events in the Q^2 region is identified by tagging the scattered positron using BPC as written in Chapter 5. The chapter also describes how to reconstruct the kinematic variables used in this thesis. After selecting the low Q^2 events inclusively in Chapter 6, the non-diffractive contribution is subtracted statistically in Chapter 7. The measured number of events is translated into the diffractive cross section and the $\alpha_{I\!P}(0)$ is extracted in Chapter 8. Finally, the conclusions are shown in the last chapter.

2. Diffraction

2.1 Kinematic variables

This section introduces kinematic variables which will be used later through this thesis. Fig. 2.1(a) represents a diagram of the neutral current (NC) ep scattering:

$$e + p \to e' + X. \tag{2.1}$$

The notation of four momenta of the particles is indicated in the parentheses in Fig. 2.1.

The Mandelstam variable s[9] in the ep scattering is

$$s = (k+p)^2 = 4E_e E_p + m_e^2 + m_p^2 \tag{2.2}$$

where E_e and E_p are the positron and proton beam energy, respectively. The $m_{e(p)}$ is the mass of the positron(proton). The values of E_e and E_p are 27.5 and 820 GeV resulting in the s to be $90200\,\mathrm{GeV}^2$.

The Q^2 is defined as the negative four momentum transfer squared of the positron:

$$Q^2 = -q^2 \equiv -(k-k')^2. \tag{2.3}$$

In the lowest order, the Q^2 is the virtuality of the exchanged boson and indicates how hard the ep scattering is. The exchanged bosons can be γ and Z^0 for the NC reactions. However, since the Q^2 is below $1\,\mathrm{GeV}^2$, the effect of Z^0 can be completely neglected in this thesis.

The Bjorken scaling variables x and y are defined as follows.

$$x \equiv \frac{-q^2}{q \cdot p} \tag{2.4}$$

$$y \equiv \frac{q \cdot p}{k \cdot p} \tag{2.5}$$

In the naive Quark Parton Model (QPM), x represents the fraction of momentum of the proton carried by a parton which is struck by the virtual

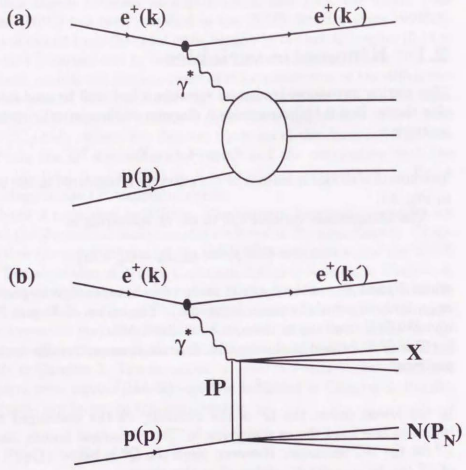

Fig. 2.1: The diagrams for (a) the general neutral current process and for (b) the diffractive process. The notation of four momenta of the particles is indicated in the parentheses.

photon. The variable y is the fraction of the incoming positron energy carried by the exchanged photon in the proton rest frame. These variables are not independent of each other and are connected with a relation,

$$Q^2 = sxy \tag{2.6}$$

where m_p^2 and m_e^2 are neglected.

The $\gamma^* p$[1] center-of-mass energy squared, W^2, can be expressed using the variables Q^2, y and s as follows:

$$\begin{aligned} W^2 &= (q+p)^2 \\ &= q^2 + 2q \cdot p + p^2 \\ &= -Q^2 + s \cdot y + m_p^2. \end{aligned} \tag{2.7}$$

In the kinematic range discussed in this thesis, all but the second term are neglected. Therefore, W can be approximated to

$$W = \sqrt{s \cdot y}. \tag{2.8}$$

As shown in Fig. 2.1(b) for the diffractive scattering, $e + p \to e' + X + N$, the hadronic system could be separated into two systems, the photon dissociative system (X) and the proton dissociative system (N). The N is the proton or a higher mass baryonic state. We need more kinematic variables to define the system.

The M_X is defined as the mass of the system which the virtual photon dissociates into. Similarly, M_N is defined as the mass of the baryonic state on the proton side.

The t is the square of the difference of momenta between incoming proton and outgoing baryonic state,

$$t = (p - p_N)^2. \tag{2.9}$$

In the view that the diffractive scattering is mediated by the Pomeron exchange[27], two more variables are used. They are defined as

$$x_{I\!P} = \frac{(p - p'(p_N)) \cdot q}{p \cdot q} \simeq \frac{M_X^2 + Q^2}{W^2 + Q^2} \tag{2.10}$$

and

$$\beta = \frac{x}{x_{I\!P}} \simeq \frac{Q^2}{Q^2 + M_X^2}. \tag{2.11}$$

The variable $x_{I\!P}$ represents the momentum fraction of the Pomeron in the incoming proton. The variable β is the momentum fraction of the struck quark in the exchanged Pomeron.

[1] The asterisk remarks explicitly that the exchanged photon is a virtual photon.

2.2 The relation of the ep and $\gamma^* p$ cross sections

The differential cross section on Q^2 and y of the ep scattering can be written as

$$\frac{d^2\sigma_{ep}}{dQ^2dy} = \frac{2\pi\alpha^2 Y_+}{yQ^4}\left\{F_2 - \frac{y^2}{Y_+}(F_2 - 2xF_1)\right\} \tag{2.12}$$

where $Y_+ = 1+(1-y)^2$ and F_1 and F_2 are dimensionless structure functions of the proton. The QPM regards the ep scattering as the scattering of the electron and a quark in the proton, neglecting the transverse momentum and mass of the quark[1]. In QPM, the structure functions are related as

$$2xF_1(x,Q^2) = F_2(x,Q^2) = \sum_i e_i^2 f_i(x) \tag{2.13}$$

where e_i and $f_i(x)$ are the charge and the probability density function of the parton i.

If the electron is regarded as a source of the transversely and longitudinally polarized photon, the cross section of the ep scattering can be written in terms of the $\gamma^* p$ cross sections, $\sigma_T^{\gamma^* p}$ and $\sigma_L^{\gamma^* p}$, as follows[2]:

$$\frac{d^2\sigma_{ep}}{dQ^2dy} = \Gamma \cdot \sigma_T^{\gamma^* p} \cdot (1+\epsilon R) \tag{2.14}$$

where the Γ and ϵ represent

$$\Gamma = \frac{\alpha(1+(1-y)^2)}{2\pi Q^2 y} \tag{2.15}$$

and

$$\epsilon = \frac{2(1-y)}{1+(1-y)^2}. \tag{2.16}$$

The R in (2.14) stands for the ratio of the longitudinal to transverse $\gamma^* p$ cross sections:

$$R = \sigma_L^{\gamma^* p}/\sigma_T^{\gamma^* p} \tag{2.17}$$

Similarly, in terms of the transverse and longitudinal $\gamma^* p$ diffractive cross sections, the ep diffractive cross section can be written as

$$\frac{d^3\sigma_{ep}^{diff}}{dQ^2dydM_X} = \Gamma \cdot \frac{d(\sigma_T^{diff} + \epsilon\sigma_L^{diff})}{dM_X}. \tag{2.18}$$

Therefore, the $\gamma^* p$ diffractive cross section can be obtained from the ep cross section as

$$\begin{aligned}\frac{d\sigma_{\gamma^* p}^{diff}}{dM_X} &= \frac{d(\sigma_T^{diff} + \sigma_L^{diff})}{dM_X} \\ &= \frac{1+R^{diff}}{1+\epsilon R^{diff}} \cdot \frac{1}{\Gamma} \cdot \frac{d^3\sigma_{ep}^{diff}}{dQ^2dydM_X}\end{aligned} \tag{2.19}$$

where $R^{diff} = \sigma_L^{diff}/\sigma_T^{diff}$. As discussed in Chapter 8, the factor $(1+R^{diff})/(1+\epsilon R^{diff})$ can be approximated to unity because $\epsilon \simeq 1$ in the considered y range in this thesis.

2.3 Diffractive cross section

2.3.1 Hadronic behaviour of the virtual photon

In the previous section, the cross section of the ep scattering was related to that of the $\gamma^* p$ scattering. From this section, we look into the characteristics of the $\gamma^* p$ cross section itself.

Although the term '$\gamma^* p$ scattering' has been used up to now, it is also possible that the virtual photon fluctuates into a $q\bar{q}$ state by the uncertainty principle. Vector mesons, for example ρ^0, ω and ϕ, are the $q\bar{q}$ states whose quantum numbers are the same as those of the photon. In the framework of Vector meson Dominance Model (VDM)[28], the cross section of the vector meson and proton scattering dominates rather than that of the bare photon and proton scattering. It can be seen as follows.

The energy difference between the virtual photon and the vector meson into which the photon fluctuates is obtained as

$$\Delta E \sim \frac{Q^2 + M_V^2}{2E_{\gamma^*}}. \tag{2.20}$$

From the uncertainty principle, the lifetime of the vector meson is given as the inverse of ΔE. If the Q^2 and M_V^2 are small enough, the lifetime of the $q\bar{q}$ state becomes long and the path length becomes long compared with the size of nucleons ($\sim$1fm)[29]. In the small Q^2 range ($Q^2 < 1\,\mathrm{GeV}^2$), the scattering of the virtual photon and proton could be treated using the formalisms for hadron-hadron collisions.

2.3.2 The $\gamma^* p$ diffractive processes

As seen in Fig. 2.2, the $\gamma^* p$ diffractive scattering can be classified into four

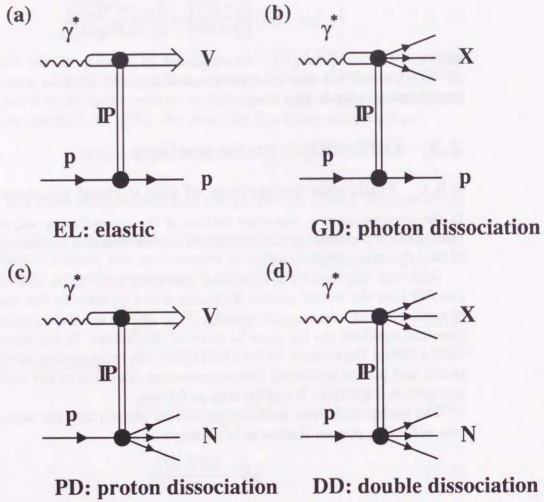

Fig. 2.2: The diffractive processes observed in the $\gamma^* p$ scattering, (a)elastic scattering, (b)single photon dissociation, (c)single proton dissociation and (d)double dissociation.

processes, depending on the final states of the photon and proton:

Elastic scattering (EL) $\gamma^* + p \to V + p$:

The photon fluctuates to a vector meson and scatters off the proton elastically.

Single photon dissociation (GD) $\gamma^* + p \to X + p$:

The photon (vector meson) is dissociated into the higher mass state (X) while the proton stays intact.

Single proton dissociation (PD) $\gamma^* + p \to V + N$:

The vector meson stays intact but the proton is dissociated into the higher mass state (N).

Double dissociation (DD) $\gamma^* + p \to X + N$:

Both the photon and proton are dissociated into the higher mass states.

2.3.3 Regge theory and the elastic cross section

This section shows the analytic behaviour of the hadron-hadron elastic scattering according to the Regge theory[8].

Suppose a hadron-hadron elastic scattering, $A + B \to A + B$, which is mediated by a hadron exchange as depicted in Fig. 2.3(a). Mandelstam variables[9] for the scattering are defined as follows:

$$s = (p_A + p_B)^2 = (p'_A + p'_B)^2 \tag{2.21}$$

$$t = (p_A - p'_A)^2 = (p_B - p'_B)^2 \tag{2.22}$$

The hadron-hadron scattering cannot be explained by an exchange of single kind of known particle. It should be the superposition of particles with different spins as illustrated in Fig. 2.3(b). In the Regge theory, the superposition of them is regarded as a Reggeon exchange.

Fig. 2.4 which is called Chew-Frautschi plot[30] shows the correlation between spin and mass of Reggeons. It shows that Reggeons are on a trajectory (Reggeon trajectory) which is approximated to a linear function:

$$\alpha(t) = \alpha(0) + \alpha' t. \tag{2.23}$$

For the most of the Reggeon trajectories, the slope α' is known to be about 1[31]. The extracted values of the intercept of trajectories are summarized in Tab. 2.1.

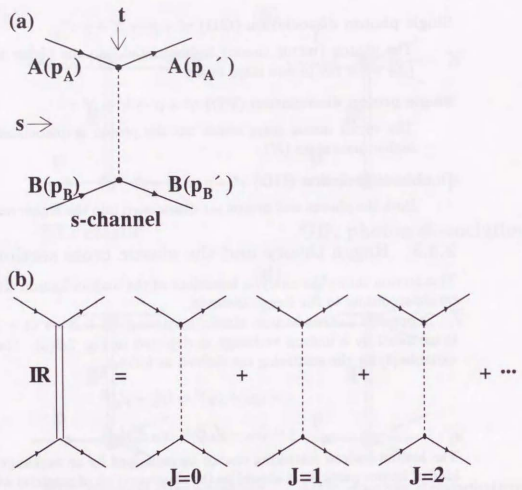

Fig. 2.3: (a)The diagram of process $A + B \to A + B$. (b)The process is described as the exchange of a Reggeon, which is a composite state of different spin particles.

process	t-channel	$\alpha(0)$
$\pi^- p \to \pi^0 n$	ρ	0.5
$K^- p \to \bar{K}^0 n$	ρ, a_2	0.5
$\gamma p \to \pi^0 p$	ρ, ω	0.5
$\pi^- p \to K^0 \Lambda$	K^*, K_2^*	0.2
$K^- p \to \pi^0 \Lambda$	K^*, K_2^*	0.2
$\pi^- p \to p\pi^-$	Δ	0
$\pi^+ p \to p\pi^+$	N, Δ	0

Tab. 2.1: The extracted values of $\alpha(0)$[31].

According to the Regge theory, the s dependence of the amplitude at the fixed t can be written as

$$\mathcal{A}(s \to \infty, t) \sim \beta(t) s^{\alpha(t)} \tag{2.24}$$

and the cross section of the elastic scattering, $A + B \to A + B$, at the fixed t can be expressed as

$$\frac{d\sigma}{dt} \sim \frac{|\mathcal{A}(s,t)|^2}{s^2} \sim F(t) \left(\frac{s}{s_0}\right)^{2\alpha(t)-2} \tag{2.25}$$

where $s_0 \simeq 1\text{GeV}^2$ is the hadron mass scale.

For example, in the pp and $p\bar{p}$ elastic scattering experiments[32, 33, 34, 35], it was observed that the cross section is peaked at $|t|$ =0 and falls exponentially as increasing $|t|$:

$$\frac{d\sigma}{dt} \propto e^{Bt}. \tag{2.26}$$

Also at HERA, the exponential behaviour of t was observed in the elastic ρ^0 production process[36, 37, 38]. Those experimental results lead us to write down the $F(t)$ in (2.25) as $F(t) = Fe^{bt}$. By substituting it into (2.25), the cross section can be rewritten as

$$\frac{d\sigma}{dt} = F\left(\frac{s}{s_0}\right)^{2\alpha(0)-2} \exp\left\{\left(b + 2\alpha' \ln\left(\frac{s}{s_0}\right)\right) t\right\}. \tag{2.27}$$

As seen in the above formula, the exponential slope becomes steeper as the center-of-mass energy increases. This phenomenon is originated from the slope (α') of trajectories and it is usually called 'shrinkage'[8]. The shrinkage is the characteristic of the Regge phenomenology.

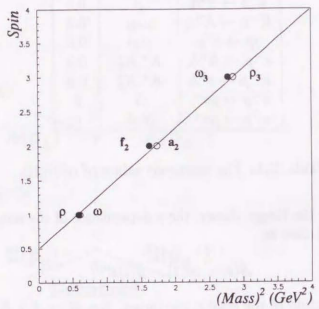

Fig. 2.4: Chew-Frautschi plot of a Reggeon trajectory.

2.3.4 Total cross section and soft Pomeron

According to the optical theorem[1], the imaginary part of the forward(t=0) elastic scattering amplitude is related to the total cross section as follows:

$$\sigma_{tot}(AB \to X) \sim \frac{1}{s} Im\mathcal{A}(AB \to AB, s, t=0). \tag{2.28}$$

Therefore, the s dependence of the total cross section can be expressed as

$$\sigma_{tot}(AB \to X) \propto s^{\alpha(0)-1}. \tag{2.29}$$

The data of various kinds of hadron-hadron collisions are now available[11]. In high energy hadron-hadron collisions, the total cross sections turned out to be almost constant as a function of s. In order to describe such s dependence within the framework of the Regge picture, another trajectory whose intercept is about 1 is necessary in addition to the known trajectories. The trajectory is called Pomeron trajectory and it is assumed to have the form,

$$\alpha_{I\!P}(t) = \alpha_{I\!P}(0) + \alpha'_{I\!P} \cdot t \tag{2.30}$$

where the $\alpha'_{I\!P}$ is required to be 0.25±0.02 from the slope of $d\sigma/dt$ of the pp elastic scattering[39].

A.Donnachie and P.V.Landshoff[12] successfully fitted the total cross sections (mb) to the form,

$$\sigma_{tot} = Xs^{\epsilon} + Ys^{-\eta} \tag{2.31}$$

where the first and second terms represent the Pomeron and Reggeon exchanges, respectively. For the γp scattering, they obtained as

$$\sigma_{tot}^{\gamma p} = 0.0677 s^{0.0808} + 0.129 s^{-0.4525} \tag{2.32}$$

using the data collected at $\sqrt{s} < 20$GeV. The Pomeron with $\alpha_{I\!P}(0)$ =1.0808 is referred to as soft Pomeron. At HERA, this prediction was examined in the higher $\sqrt{s}$ region ($\sqrt{s}$ ~200GeV). The total photoproduction cross section measured by ZEUS[13] and H1[14] turned out to be consistent with the soft Pomeron.

2.3.5 Diffractive cross section at triple Regge limit

The cross section of the photon dissociative diffraction, $\gamma^* + p \to X + p$, can be obtained by means of the Mueller's theorem[40]. It is the generalized optical theorem and relates the inclusive process, $AB \to CX$, to the amplitude of the three-body forward elastic scattering, $AB\bar{C} \to AB\bar{C}$. It is represented pictorially in Fig. 2.5.

Let us think of only the limited case: $M_X^2 \to \infty$ and $W^2/M_X^2 \to \infty$. This is called triple Regge limit[8]. As far as the triple Regge limit is concerned, the cross section of the inclusive diffraction is expressed as

$$\frac{d^2\sigma}{dtdM_X^2} = \left(\frac{1}{W^2}\right)^2 \cdot G_{ijk}(t) \left(\frac{W^2}{M_X^2}\right)^{\alpha_i(t)+\alpha_j(t)} M_X^{2\alpha_k(0)} \tag{2.33}$$

where suffixes i, j and k represent the trajectories and the G_{ijk} is the coupling strength[15]. We only take into consideration that i and j are Pomerons because the Reggeon contribution is negligible in our W region as seen in the previous section. If the trajectory k is also a Pomeron, the cross section is proportional to ~$1/M_X^2$. On the other hand, if the k is a Reggeon, the cross section is proportional to ~$1/M_X^3$ because $\alpha_{I\!R}$ ~0.5. In both cases, the W dependence becomes

$$\frac{d^2\sigma}{dtdM_X^2} \propto (W^2)^{2\alpha_{I\!P}(t)-2} \tag{2.34}$$

which is similar to the cross section of the elastic scattering seen in (2.27).

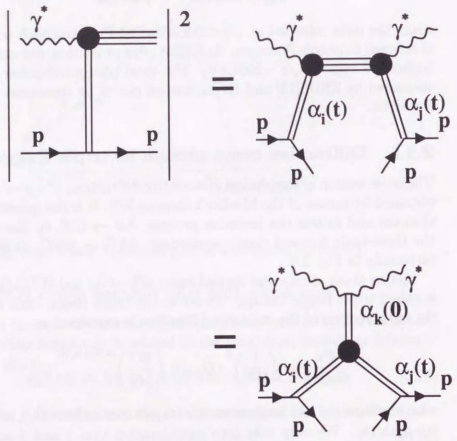

Fig. 2.5: The inclusive photon dissociation and the elastic three-body forward amplitude.

3. Experimental setup

3.1 HERA

HERA (Hadron Elektron Ring Anlage) is the first electron-proton collider in the world constructed at DESY (Deutsches Elektronen-Synchrotron) in Hamburg, Germany. The layout of HERA is shown in Fig. 3.1. The main design parameters of HERA are listed in Tab. 3.1.

HERA was operated with 820 GeV protons and 27.5 GeV positrons in the 1996 data taking period. The center-of-mass energy is, therefore, equal to 300 GeV. The typical currents of the proton and positron beams were about 50 and 25 mA, respectively, and the maximum luminosity reached $1.0 \times 10^{31}\,\mathrm{cm}^{-2}\mathrm{s}^{-1}$.

There are four experimental sites along the HERA ring. The ZEUS detector is located at the South Hall.

3.2 ZEUS Detector

The ZEUS detector[41] is a multipurpose apparatus to reconstruct events from *ep* collisions. An overview of the detector is shown in Fig. 3.2. The coordinate system used in the ZEUS experiment is defined as the following way. The origin of the coordinate is at the nominal interaction point. The z-axis is identical with the nominal beam axis, and the positive(forward) and negative(rear) directions are the proton and positron beam directions, respectively. The positive x-axis is the horizontal direction toward the center of the HERA ring, and the positive y-axis is the upward direction.

As shown in Fig. 3.2, the shape of the ZEUS detector is asymmetric in z-direction because of the large energy difference between the proton and positron beam. This energy imbalance makes the center-of-mass system boosted, and more particles are emitted to the forward direction.

The important components in this analysis are the uranium-scintillator calorimeter (CAL), the central tracking detector (CTD), the beam pipe calorimeter (BPC), the proton remnant tagger (PRT) and the luminosity monitor (LUMI).

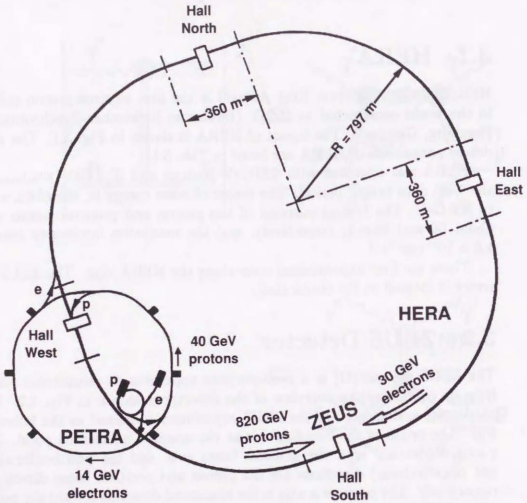

Fig. 3.1: The HERA *ep* collider.

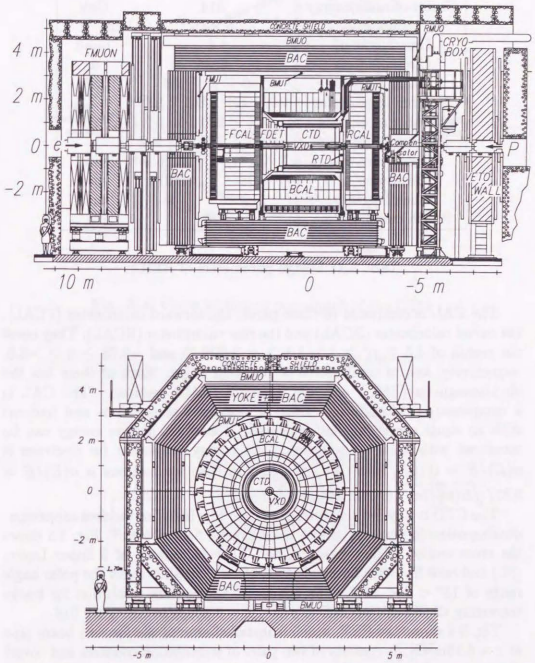

Fig. 3.2: Cross sections of the ZEUS detector along and perpendicular to the beam direction.

	proton	electron	unit
Beam energy	820	30	GeV
Center-of-mass energy	314		GeV
Luminosity	1.5×10^{31}		$cm^{-2}s^{-1}$
Crossing angle	4		mrad
Circumference	6336		m
Beam current	160	58	mA
Number of particles	2.1×10^{13}	0.8×10^{13}	
Number of buckets	220		
Number of bunches	210		
Beam size σ_x	0.27	0.26	mm
Beam size σ_y	0.08	0.07	mm
Bunch length σ_z	110	8	mm
Bunch crossing time	96		ns

Tab. 3.1: Design parameters of HERA.

The CAL is composed of three parts: the forward calorimeter (FCAL), the barrel calorimeter (BCAL) and the rear calorimeter (RCAL). They cover the region of $4.3 \geq \eta^1 \geq 1.1$, $1.1 \geq \eta \geq -0.75$ and $-0.75 \geq \eta \geq -3.8$, respectively, and in total 99.7% of the solid angle. Each of them has the electromagnetic (EMC) and the hadronic (HAC) sections. The CAL is a compensated calorimeter. That is, responses of electrons and hadrons with an equal energy are almost equal. Therefore, hadron energy can be measured with a high resolution. The energy resolution for electrons is $\sigma(E)/E = 0.18/\sqrt{E(in\ GeV)} \oplus 0.02$ and that for hadrons is $\sigma(E)/E = 0.35/\sqrt{E(in\ GeV)} \oplus 0.02$ at the test beam.

The CTD is a cylindrical drift chamber. It is installed inside a supperconducting solenoid which produces the magnetic field of 1.43 T. Fig. 3.3 shows the cross section of one octant of the CTD. It consists of 9 Super Layers (SL) and each SL has 8 layers of sense wires. The SL2 covers the polar angle range of $15^o < \theta < 164^o$. The transverse momentum resolution for tracks traversing all SLs of the CTD is $\sigma(p_t)/p_t = 0.005p_t(in\ GeV) \oplus 0.016$.

Fig. 3.4 shows the PRT, which is installed around the forward beam pipe at $z = 5.15$m[42]. It consists of two pairs of scintillation counters and covers the η range of $4.0 < \eta < 6.0$.

In the ZEUS experiment, two detectors, LUMIE and LUMIG, are mounted

[1] The η represents pseudorapidity defined as $-\ln(\tan\theta/2)$. The θ is the polar angle taken with respect to the proton beam direction from the interaction point.

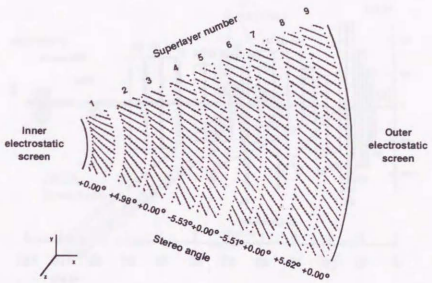

Fig. 3.3: Cross section of one octant of the CTD.

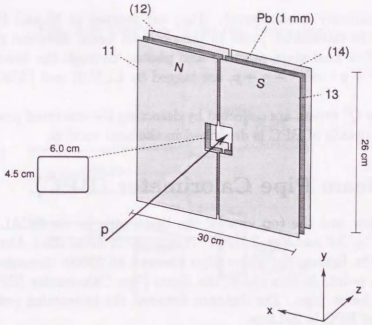

Fig. 3.4: The Proton Remnant Tagger (PRT). It consists of four scintillator tiles labeled as 11, 12 for north side and 13, 14 for south side.

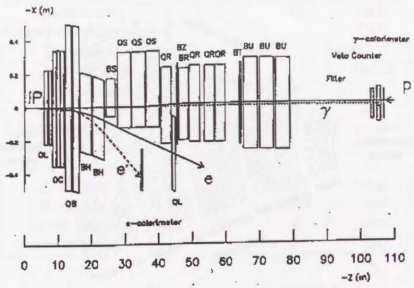

Fig. 3.5: Overview of the luminosity monitors (LUMI).

for the luminosity measurement. They are located at 35 and 108m downstream of the interaction point in the positron beam direction as shown in Fig. 3.5. The final state positron and photon through the bremsstrahlung process, $e^+ + p \longrightarrow e^+ + \gamma + p$, are tagged by LUMIE and LUMIG, respectively.

The low Q^2 events are collected by detecting the scattered positron using BPC. The details of BPC is described in the next section.

3.3 Beam Pipe Calorimeter (BPC)

The overview and the top view of the beam pipe in the RCAL region are shown in Fig. 3.6 and Fig. 3.7[25]. It is made of 5mm thick Aluminum. As shown in the figures, the beam pipe narrows at 250cm downstream of the interaction point. In this space, the Beam Pipe Calorimeter (BPC) was set beside the beam pipe. The distance between the interaction point and the front face of BPC is 293.8cm.

Fig. 3.8 shows the end view of the RCAL and the beam pipe. One calorimeter module is located on each side of the beam pipe; one in the positive x direction is referred to as BPC North (BPCN) and the other in the negative x is referred to as BPC South (BPCS). Only the BPCN is used

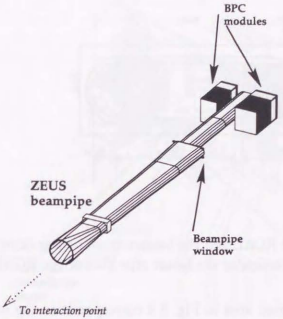

Fig. 3.6: Overview of the rear beam pipe.

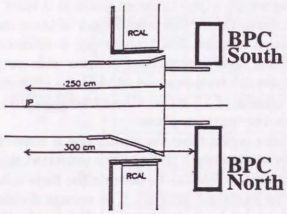

Fig. 3.7: Top view of the rear beam pipe. The horizontal scale is much reduced compared with the vertical scale.

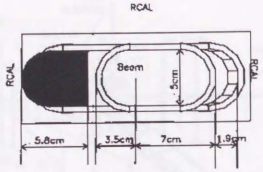

Fig. 3.8: End view of the RCAL and the beam pipe. The box drawn around the beam pipe indicates the beam pipe hole of the RCAL.

in this analysis[2]. The shaded area in Fig. 3.8 corresponds to the window of the beam pipe. In this area, it is possible to measure the energy accurately because there is little material ($\leq$0.02 radiation lengths) in front of BPC. On the other hand, particles emitted to the outside of the shaded area are forced to traverse the beam pipe diagonally. The energy of such particles cannot be measured accurately.

Fig. 3.9 is the schematic view of BPC. The box drawn in the foreground is BPCN. The module consists of 26 layers of tungsten plates and 26 layers of SCSN-38 scintillators[43]. One tungsten plate is 3.5mm thick and one scintillator layer is 2.6mm thick. The total length of these calorimeters corresponds to 22 radiation lengths. The Moliere unit is estimated to be about 13mm. Each scintillator layer is composed of 8mm wide strips[44]. Among the 26 scintillator layers, 13 layers consist of 16 strips aligned vertically, and the other 13 layers consist of 15 strips aligned horizontally. They are put alternatively between the tungsten plates.

The light in the blue region from the scintillator is converted to the light in the green region by a wavelength shifter. The converted signals are guided to HAMAMATSU R5600-03 PMTs. To provide the high-voltage for PMTs, Cockcroft-Walton type bases are used[45]. The voltage division between the dynodes are 1/2:1:1:1:1:1:1:1 which is carried out inside the high-voltage supply. The divided voltage is sent to the PMT base through a flat cable.

The assignment of PMTs is shown in Fig. 3.10. The vertical strips are referred to X1 to X15, and the horizontal ones are referred to Y1 to Y16.

[2] Later, the term 'BPC' is used for the BPCN.

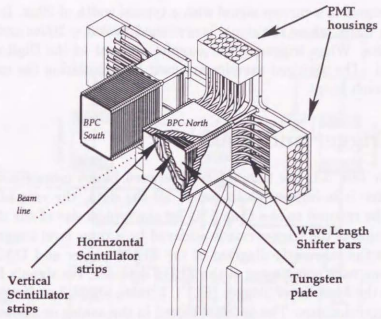

Fig. 3.9: Schematic view of the BPC module.

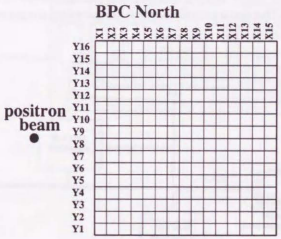

Fig. 3.10: Assignment of the BPC strips.

The PMT signal is a current signal with a typical width of 20ns. It is sent to the Analog Card, where the signal is stretched to 200 ~ 300ns and sampled in every 96ns. When triggered, the samples are sent to the Digital Card to be digitized. The digitized samples are used for calculating the energy and timing for each strip.

3.4 Trigger and DAQ

As listed in Tab. 3.1, the time interval between bunch crossings is 96 ns at HERA. Since it is impossible to record all the data, the rate of recorded data must be reduced to less than 5 Hz for the typical size of the data. This large reduction of the trigger rate is achieved by a three level trigger system. Fig. 3.11 is the schematic diagram of the ZEUS trigger and DAQ system. At first, from each component of the ZEUS detector, the signals for trigger are sent to the First Level Trigger (FLT). It takes about 5 μs for the FLT to make a trigger decision. The data are stored in the analog or degital pipeline in the meantime. The trigger rate is reduced to about 1 kHz by the FLT. At the Second Level Trigger (SLT), the trigger rate is reduced to 100 Hz mainly by timing cuts to reject the proton beam-gas backgrounds. In case the SLT makes a positive decision, the signals are sent to the Event Builder (EVB). The EVB makes the data from different components fit into a large structured format and constructs an event data. At last, the Third Level Trigger (TLT) makes more sophisticated trigger decision. The final trigger rate is a few Hz, and the data satisfying the trigger requirements are recorded on the magnetic tape.

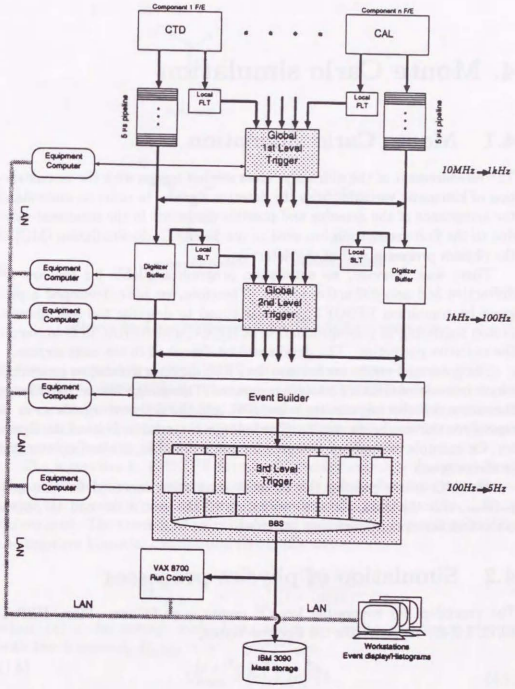

Fig. 3.11: Schematic diagram of the ZEUS trigger and DAQ system.

4. Monte Carlo simulation

4.1 Monte Carlo simulation

The measurement of the diffractive cross section begins with the reconstruction of kinematic variables from the detector signals. In order to understand the acceptance of the detector and possible distortion in the measured value due to the finite resolution, we need to use Monte Carlo simulation (MC) of the physics processes and of the detectors.

There was, however, no simulation program available for the low Q^2 diffractive and non-diffractive events. Therefore, we have developed a program by combining EPSOFT, which is tuned to describe the soft photon-proton scattering in photoproduction at HERA, and HERACLES to handle the radiative correction. The details will be described in the next section.

The generated events are fed into the ZEUS detector simulation program[46] which is made of GEANT3.13[47] programs. The energy loss of particles in the active detector regions are translated into the detector signals so as to reproduce the test beam results. The inactive material in front of the detector, for example beampipes, detector frames and cables, is also implemented in the program.

The MC events passing the detector simulation are used for the comparison with the data, for the evaluation of the resolution and to obtain correction factors on kinematic variables.

4.2 Simulation of physics processes

The procedure for generating low Q^2 events is as follows. First, HERACLES 4.6[48, 49] generates the electron vertex,

$$e^+ \to e^+ + \gamma^*(+\gamma) \tag{4.1}$$

where the γ^* means the virtual photon and the γ is the radiated photon from the incoming or outgoing positron. Example diagrams are shown in Fig. 4.1. Fig. 4.1(a) shows the diagram without QED radiation, so called Born term. The diagrams (b) and (c) are called the initial and final state

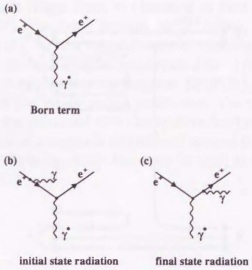

Fig. 4.1: The electron vertices HERACLES generates.

radiation, respectively. Next, the four momentum of the virtual photon is transferred to EPSOFT[50]. This is a generator which has been developed in the framework of HERWIG[51, 52] and simulates the soft interactions of the photon and the proton. It is able to generate both non-diffractive events and events from the diffractive processes shown in Fig. 2.2.

The algorithm in EPSOFT for non-diffractive events is described here. The non-diffractive process is regarded as the soft hadron interactions between the virtual photon and proton. At first, the particle multiplicity is determined. The number of pairs of charged particles, n, is characterized by the negative binomial distribution (NBD)[53, 54]:

$$P_n = \begin{pmatrix} n+k-1 \\ n \end{pmatrix} \frac{(\langle n \rangle / k)^n}{(1+\langle n \rangle / k)^{n+k}} \tag{4.2}$$

where $\langle n \rangle$ is the average multiplicity and k is a width parameter relating with the dispersion, $D_{NBD} = (n^2 - \langle n \rangle^2)^{1/2}$, as

$$D_{NBD}^2 = \langle n \rangle + \langle n \rangle^2 / k \tag{4.3}$$

The value of $1/k$ is fixed to 0.021[50]. The $\langle n \rangle$ is a function of W and parameterized as

$$\langle n \rangle = 0.21 \cdot (\log W)^2 + 0.43 \cdot \log W + 0.86. \tag{4.4}$$

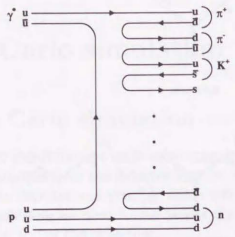

Fig. 4.2: The $q\bar{q}$ pair productions between the virtual photon and the proton. They are clustered into hadrons of the lightest mass.

The function form of $\langle n \rangle$ is suggested from $p\bar{p}$ data[55]. The parameters are tuned to the ZEUS non-diffractive photoproduction data.

After selecting the multiplicity of a generated event, $q\bar{q}$ $(q = u, d, s)$ pairs are created between γ^* and p as shown in Fig. 4.2. Then the adjacent $\bar{q}$ and q are linked to form a hadron. The hadron with the lightest mass is assigned to the $\bar{q}q$ cluster. This procedure is continued until the charged multiplicity reaches twice as many as n determined above.

The transverse momenta of the particles are generated according to the probability distribution of the form[56]:

$$\frac{dN}{dp_T^2} \propto \exp(-b \cdot \sqrt{p_T^2 + m^2}) \tag{4.5}$$

where the m denotes the mass of the particle. The slope parameter b is tuned to the ZEUS photoproduction data[57] and it is parameterized as

$$b = 2/(0.00175 \cdot (\log W)^2 + 0.00167 \cdot \log W + 0.353). \tag{4.6}$$

The longitudinal momenta are generated randomly in the rapidity space[58].

The diffractive processes can be generated similarly by EPSOFT. In these cases, the same procedure is done for $\gamma^* I\!P$ and/or $pI\!P$ system. The cross

section of the photon dissociative diffraction for $M_X \geq 1\,\mathrm{GeV}$ is calculated according to the triple Regge limit as discussed in Section 2.3.5. As shown in the formula (2.33), the cross section, $d\sigma^{diff}_{\gamma^* p}/dM_X^2$, is generated to be proportional to $\sim 1/M_X^2$ for the triple Pomeron contribution ($I\!P I\!P I\!P$). On the other hand, it is generated to be proportional to $\sim 1/M_X^3$ if the trajectory labeled as k in Fig. 2.5 is set to be a Reggeon ($I\!P I\!P I\!R$).

For the process of the vector meson production, the three kinds of vector mesons, ρ, ω and ϕ, are produced with the relative fraction of $1/2.2 : 1/13.4 : 1/23.6$ [59]. The mass of ρ meson is distributed around 0.7681GeV according to the Breit-Wigner formula, while the mass of $\omega(\phi)$ is fixed to a constant, 0.7819(1.0194)GeV[11].

5. Reconstruction of kinematic variables

5.1 Introduction

In order to measure the inclusive diffractive cross section, it is necessary to reconstruct kinematic variables Q^2, W and M_X using signals from components of the detector. For the kinematic region considered in this thesis, the Q^2 and W are reconstructed from the measured energy and scattered angle of the final state positrons in BPC. On the other hand, M_X and other quantities describing hadronic final states are obtained from the CAL and CTD information. The detailed explanations of those reconstruction methods are presented in the next sections.

5.2 Reconstruction of Q^2 and W

The kinematic variables Q^2 and W can be obtained from the precise measurement of the scattered positrons. The method is called electron method and the variables can be calculated as follows:

$$Q^2_{el} = 2E_e E_{e'}(1 + \cos\theta_{e'}) \tag{5.1}$$

$$W_{el} = \sqrt{s \cdot y_{el}} \tag{5.2}$$

$$y_{el} = 1 - \frac{E_{e'}}{2E_e}(1 - \cos\theta_{e'}) \tag{5.3}$$

where $E_{e'}$ and $\theta_{e'}$ mean the energy and polar angle of the scattered positron. The E_e is the energy of initial state positron and the definition of s was shown in (2.2). In the following sections, the reconstruction of the scattered positron in BPC is described.

On the other hand, a significant portion of hadronic particles emitted after the scattering is caught in the main detector. The kinematic variables can also be reconstructed from them. For example, y can be extracted from Jacquet-Blondel method[60]. It is referred to as y_{JB}. In the kinematics of

this study, the resolution is better to use only the electron method. The y_{JB} is used in the selection cut.

5.3 Reconstruction of the positron in BPC

5.3.1 BPC position measurement

The measurement of the scattered angle $\theta_{e'}$ is started from the local hit position of the scattered positron in BPC. As shown in Fig. 3.10, the BPC North module is composed of 15 vertical and 16 horizontal strips. This structure enables us to calculate the horizontal and vertical local position independently.

For the local position reconstruction, the logarithmic weighted method is adopted [61, 62]. The horizontal local position, x_l, is calculated as

$$x_l = \frac{\sum_{i=1}^{15} w_i x_i}{\sum_{i=1}^{15} w_i} \tag{5.4}$$

where x_i denotes each center position of the i-th strip. The w_i is a weighting factor for the i-th strip and defined as

$$w_i = \begin{cases} w_0 + \ln(\frac{E_{Xi}}{E}) & (E_{Xi} > Ee^{-w_0}) \\ 0 & (E_{Xi} \leq Ee^{-w_0}) \end{cases} \tag{5.5}$$

where E_{Xi} denotes energy deposit on i-th strip and E is the total energy deposited on vertical strips. The value of w_0 was determined to minimize the position resolution[62]. The optimized value was 2.8. The vertical position, y_l, can be calculated in the similar way:

$$y_l = \frac{\sum_{i=1}^{16} w_i y_i}{\sum_{i=1}^{16} w_i}. \tag{5.6}$$

Fig. 5.1 is the local position distribution in BPC seen from the interaction point. Although the outer rectangle in the figure indicates the BPC North module, the local positions are distributed only in the specific region. This is due to the trigger requirement as described below.

As shown in Fig. 3.6 and Fig. 3.7, there is a window to BPC at the end of the beam pipe. It is possible to measure the energy and position well only if the positron arrives at BPC after passing the window which is made of a material with less than 0.02 radiation length. The trigger logic is set to get the positrons in the fiducial volume shown as a hexagon in Fig. 5.1. As mentioned in Section 6.3.1, only the events whose BPC local position is

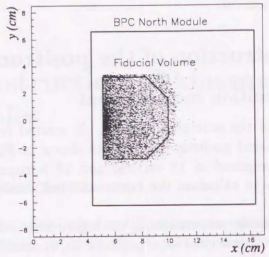

Fig. 5.1: Reconstructed local positions in BPC seen from the interaction point. The outer rectangle shows the BPC module and inner one indicates the fiducial volume used in this analysis.

within the fiducial volume will be used for extracting the diffractive cross section.

The dispersion of each local position is defined as

$$\sigma_x^2 = \frac{\sum_{i=1}^{15} w_i x_i^2}{\sum_{i=1}^{15} w_i} - x_l^2 \tag{5.7}$$

and

$$\sigma_y^2 = \frac{\sum_{i=1}^{16} w_i y_i^2}{\sum_{i=1}^{16} w_i} - y_l^2. \tag{5.8}$$

They represent the spread of lateral shower profiles for x and y directions. In case a hadron enters BPC, the shower would grow wider than typical electromagnetic showers. The values of σ_x and σ_y will be used for rejecting hadrons misidentified as scattered positrons.

5.3.2 BPC timing measurement

The arrival timing of the particle to BPC is reconstructed as the linear energy weighted mean of the timing informations from all strips. The BPC timing,

t_{BPC}, is calculated as

$$t_{BPC} = \frac{\sum_{i=1}^{15} E_{Xi} t_{Xi}}{\sum_{i=1}^{15} E_{Xi}} + \frac{\sum_{j=1}^{16} E_{Yj} t_{Yj}}{\sum_{j=1}^{16} E_{Yj}} \tag{5.9}$$

where t_{Xi} and t_{Yj} are timing obtained from i-th vertical and j-th horizontal strips, respectively. The timing resolution is about 0.5ns.

5.3.3 BPC energy measurement

In this section, the energy reconstruction of the scattered positron using BPC is described.

The energy of the scattered positron observed in BPC is calculated by summing up energy deposits on 4 vertical strips and those on 4 horizontal strips,

$$\begin{aligned} E_{BPC} &= E_X + E_Y \\ &= c_x \sum_{4strips} E_{Xi} + c_y \sum_{4strips} E_{Yj} \end{aligned} \tag{5.10}$$

where the coefficients c_x and c_y determine the absolute energy scale of BPC. The four strips for energy reconstruction are selected as follows. First, the strip with the maximum energy deposit is searched for among all the strips for each direction. Suppose it is the i-th strip of the vertical strips, Xi. The neighboring strips, that is, $X(i-1)$ and $X(i+1)$ are also used for the sum. Then, either $X(i-2)$ or $X(i+2)$ with larger energy deposit is chosen as the last forth strip. One strip is 8mm wide. Therefore, four strips for one direction is wide enough because Moliere unit of BPC is about 13mm.

The relative gains between different strips are adjusted by taking into account the radiation damage, light attenuation along strips and shower leakage from the inner edge of BPC[62, 63, 64]. The achieved gain uniformity over the BPC fiducial volume is estimated with the scattered positrons in a special kinematics as described in Appendix A. As shown in Fig. 5.2, the uniformity inside the fiducial volume is measured to be within 0.5%. As described in Appendix B, the uncertainty of the BPC absolute energy scale is estimated with the scattered positron in the exclusive vector meson production. The absolute energy scale is determined better than 1%. The energy resolution is consistent with the test beam results, $\sigma/E \cong 0.17/\sqrt{E(in\ GeV)} \oplus 0.02$.

5.3.4 Vertex determination

In order to calculate the kinematic variables according to the electron method, the vertex position of the ep scattering is needed to be known in addition to

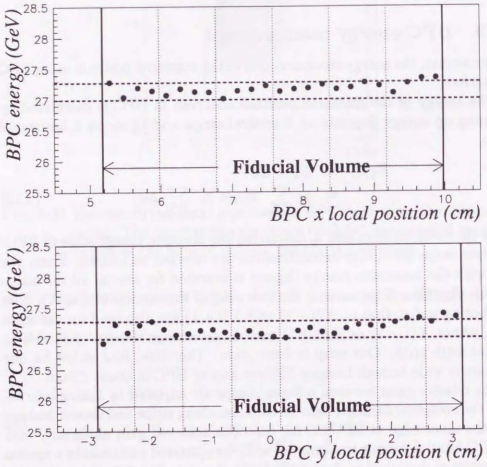

Fig. 5.2: The energy uniformity of the BPC North module. The upper and lower figures show the measured energy vs horizontal and vertical positions, respectively. The uniformity is measured to be within ±0.5 %(broken lines) in the fiducial volume.

the location of the scattered positron in BPC.

The z vertex position is determined from the CTD tracks. Since the scattered positron detected in BPC travels outside of the CTD acceptance, the vertex determination totally relies on the hadronic final states. There need to be at least one track in CTD to determine the vertex position. For the events containing more than two tracks in CTD, the resolution of the z vertex position is about 4mm. If there is no track that is compatible with the beam line, the average value of −3.3cm in the 1996 runs is regarded as the z vertex position of the event.

In principle, the x and y vertex position can be reconstructed by means of CTD. However, the resolution is about 1mm, which is much larger than the lateral spread of the beams, $\mathcal{O}(10\mu\text{m})$. For the x and y vertex positions, we take the mean values of the CTD vertex of each run.

5.3.5 Scattered angle of the positron

The scattered angle of the positron is calculated using the information of local positions, survey values and the vertex position as described below.

See Fig. 5.3 which is the top view of BPC and the positron beam line. A trajectory of the scattered positron hitting BPC is also drawn in it. In addition, there are three points, O', P and Q in the figure.

- $O'(x_v, y_v, z_v)$: the vertex position.
- $P(x_p, y_p, z_p)$: a position at the maximum energy deposition.
- $Q(x_q, y_q, z_q)$: an impact position on the BPC front face.

The local positions, x_l and y_l, measured in (5.4) and (5.6) just correspond to x_p and y_p in the BPC local coordinate system. Fig. 5.4 shows some survey values for the BPC absolute position with an accuracy of 0.5mm. They are measured from z-axis of the ZEUS coordinate; the edge of the innermost sintillator is 4.38cm away from the axis horizontally and the vertical center of BPC is placed 0.17cm higher than the axis. Therefore, the effective position of x_p and y_p(cm) can be calculated as

$$\begin{cases} x_p = x_l + 4.38 \\ y_p = y_l + 0.17. \end{cases} \tag{5.11}$$

As depicted in Fig. 5.3, x_p and y_p correspond to the x and y positions at the depth where the energy deposition profile of the electromagnetic shower

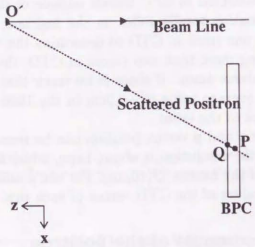

Fig. 5.3: Top view of BPC and the positron beam line.

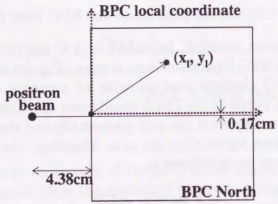

Fig. 5.4: Survey values for the absolute BPC position

becomes the maximum. The average depth, t_{max}(rl), depends on the particle energy[11]. For electrons or positrons, it is known to be

$$t_{max} = \ln(E_{e'}/E_c) - 0.5 \tag{5.12}$$

where E_c denotes the critical energy of BPC and it is 10.6MeV. Hence, the impact position on the BPC front face is obtained as follows.

$$\begin{cases} x_q - x_v = (x_p - x_v) \cdot \frac{z_q}{z_q + t_{max} \cdot 0.7} \\ y_q - y_v = (y_p - y_v) \cdot \frac{z_q}{z_q + t_{max} \cdot 0.7} \end{cases} \tag{5.13}$$

The value of z_q is known to be 293.8cm from the survey. Now we know the direction of the scattered positron with respect to the beam line. The azimuthal and polar angle of the scattered positron with respect to the beam line can be expressed as

$$\theta_{e'} = \pi - \arctan \frac{\sqrt{(x_q - x_v)^2 + (y_q - y_v)^2}}{|z_q - z_v|} \tag{5.14}$$

and

$$\phi_{e'} = \arctan \frac{(y_q - y_v)}{(x_q - x_v)}. \tag{5.15}$$

In order to obtain the kinematic variables, we need to determine the direction of the incoming positron because the positron beam was tilted inwards of the HERA ring with respect to the ZEUS z-axis. It is measured from the direction of the bremsstrahlung photons as described in Appendix C. Therefore, Q^2_{el} and W_{el} are calculated as

$$Q^2_{el} = 2E_e E_{e'}(1 + \cos\theta_{e'}) + 2\Delta p_x \sin\theta_{e'} \cos\phi_{e'} \tag{5.16}$$

and

$$W_{el} = \sqrt{4E_e E_p (1 - \frac{E_{e'}}{2E_e}(1 - \cos\theta_{e'}))} \tag{5.17}$$

where Δp_x(=0.0075 GeV) is the x component of the incoming positron momentum.

5.4 Hadronic final state

5.4.1 Overview

As seen in the previous section, Q^2 and W are reconstructed using the scattered positron detected in BPC. On the other hand, the mass of the dissociated photon, M_X, is a pure hadronic variable, which ought to be reconstructed using central components of the ZEUS detector, CAL and CTD.

At first, in this section, the uranium noise remaining in signals from CAL is taken care to obtain M_X accurately. After that, a clustering method is introduced; cells of CAL and tracks in CTD are clustered into objects each of which is regarded as one particle. The objects are used for the reconstruction of variables, M_X, y_{JB}, δ and so on, that describe hadronic final states.

5.4.2 Uranium noise suppression

Before discussing the clustering method and reconstruction of hadronic variables, this subsection is devoted to describe how to remove noisy cells in CAL from the reconstruction. Most of the noisy cells are induced by radioactivity of uranium plates which are interleaved between scintillators in CAL. This kind of noise is called 'uranium noise'. It is very important to reduce them before clustering because such unphysical cells would be also regarded as physical objects and they would cause overestimation of M_X, especially at low M_X.

At the beginning of the event reconstruction, EMC(HAC) cells with the energy less than 60(110)MeV is set to zero energy. The threshold corresponds to a cut-off at 4σ of the distribution of uranium noise[65]. This zero suppression reduce the uranium noise effect significantly but, as seen later, the effect is still visible. In order to suppress the remaining noise, higher energy thresholds were set if the cells were isolated from other cells[66, 67]. The thresholds were optimized using random trigger events.

The upper figure in Fig. 5.5 shows the average number of cells in one random trigger event as a function of the cut values for isolated EMC cells. As displayed in the upper figure, the different symbols mean different threshold values for isolated HAC cells. If the thresholds for EMC and HAC cells are 80 and 140 MeV, about 1.4 noisy cells are contaminated in one event. As can be seen in the figure, the number of noisy cells decreases rapidly as increasing the EMC threshold .

The lower figure shows the average number of noisy cells simulated in one MC event. Though the noise is not necessarily simulated enough in MC, the trend against the threshold values is similar with that observed in the random trigger data. For both data and MC, the number of noisy cells could be reduced to much below one if thresholds were high enough. In this analysis, the reconstruction is started after the isolated EMC(HAC) cells with energy less than 120(160)MeV are removed from reconstruction.

How do the higher thresholds improve the M_X reconstruction? This can be seen with elastic ρ^0 candidates in data selected in Appendix B. Fig. 5.6 shows M_X distributions for which different energy thresholds are applied. The M_X is reconstructed from energy flow objects explained in the next

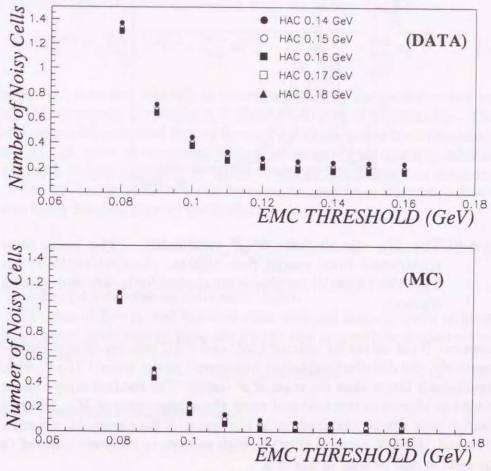

Fig. 5.5: The average number of cells in one event as a function of cut values for isolated EMC cells. Symbols indicate thresholds for isolated HAC cells shown in the upper figure. The upper figure is the average number of cells in one random trigger event. The lower figure is the average number of simulated noisy cells in one MC event.

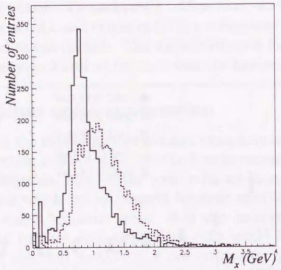

Fig. 5.6: The M_X distributions of ρ^0 candidates. The mass is reconstructed from energy flow objects. Low(80/140MeV) and high(120/160MeV) thresholds are applied for broken and solid histograms.

subsection. If cut values for isolated EMC and HAC cells are 80 and 140MeV respectively, the distribution(dotted histogram) peaks around 1GeV, which is significantly larger than the mass of ρ^0 meson. The residual noisy cells are regarded as objects in this case and cause the overestimate of M_X. However, a clear ρ^0 peak can be obtained (solid histogram) if the thresholds are raised to 120 and 160MeV because they are high enough to suppress most of the noisy cells as can be seen in Fig. 5.5.

5.4.3 Energy flow objects

For extracting the cross section of diffractive scattering, $\gamma^* + p \longrightarrow X + N$, it is necessary to measure the mass of system X which the virtual photon dissociates into. This is because the cross section will be extracted after subtracting the contribution of non-diffractive backgrounds using the shape of M_X distributions.

In principle, it is possible to reconstruct M_X only from energy deposits in CAL cells[68]. However, the resolution of M_X would be improved if one also uses CTD tracks. This is because the momentum resolution of CTD is

better than the energy resolution of CAL for low energy particles[69, 23]. In addition, one can gain the charged particles which did not reach CAL but were observed in CTD. According to the procedure explained in Appendix D, both energy deposits on CAL and tracks in CTD are clustered into objects. They are referred to as 'energy flow objects' and each of them is regarded as a particle. The M_X is reconstructed from the energy flow objects as

$$M_X^{meas} = \sqrt{(\sum_{obj} E^{obj})^2 - (\sum_{obj} p_x^{obj})^2 - (\sum_{obj} p_y^{obj})^2 - (\sum_{obj} p_z^{obj})^2}. \tag{5.18}$$

In general, however, real M_X is not reproduced by the reconstructed mass, M_X^{meas}, completely. Typically it is about 70 to 80% of the true M_X. This is because particles emitted to very forward direction escape from the detection of CAL. In order to compensate it, it is necessary to multiply additional correction factors to M_X^{meas}. It will be discussed in Chapter 7 in more detail.

The kinematic variable y can be reconstructed from the energy flow objects using Jacquet-Blondel method[60]:

$$y_{JB} = \frac{\sum_i (E - p_z)_i}{2E_e}. \tag{5.19}$$

The subscript i denotes an individual object.

The sum of $E - p_z$ over the final state particles must be twice as large as the positron beam energy from the energy and momentum conservation. It is reconstructed as

$$\delta = \sum_i (E - p_z)_i + 2E_{BPC} \tag{5.20}$$

where i denotes an individual object.

6. Event selection

6.1 Introduction

This chapter describes how the events for this analysis were selected among the whole 1996 data. It starts from the trigger condition which is designed for getting low Q^2 events inclusively. The trigger efficiency is studied with the data triggered independently. Then the offline selection criteria are described. Finally, the Q^2 and W regions to be used are determined from their distributions and resolution.

6.2 Trigger

6.2.1 FLT BPC inclusive trigger

As already mentioned in Chapter 3, the ZEUS DAQ system is composed of three level triggers. In order to take low Q^2 events inclusively, we required some conditions of BPC energy and timing at the first level trigger.

For this purpose, a fraction of raw signals from PMTs were split and they were formed to several sets of sums as listed in Tab. 6.1. During the 1996 running period, the sum over signals from horizontal strips (HORIZONTAL SUM) was used for the trigger decision.

The summed signals were led to the FADC and TDC. The FADC measures the energy by digitizing the pulse height of the signal. The timing is measured by using the TDC[70, 71] which supplies timing information with 12 counts of outputs. At the first level trigger, we required the following

VERTICAL SUM	X2+X3+...+X10
HORIZONTAL SUM	Y3+Y4+...+Y14
INNER SUM	X1
OUTER SUM	X11+...+X15+Y1+Y2+Y15+Y16

Tab. 6.1: Definition of the signal sums for trigger.

conditions:

$$(4 \leq ADCh) \cap (1 \leq TDCh \leq 7) \tag{6.1}$$

where ADCh and TDCh mean ADC and TDC outputs of horizontal sums.

Fig. 6.1 shows the distributions of ADC and TDC outputs and their correlations with the reconstructed energy and timing. From the lower left figure, a clear correlation between ADC outputs and BPC energy can be seen. The logic, $4 \leq ADCh$, corresponds that the BPC energy should be greater than about 5GeV. The correlation between TDC outputs and BPC timing is shown in the lower right of Fig. 6.1. Here 'BPC timing=0' is adjusted to the timing due to a particle from ep collision. The logic, $1 \leq TDCh \leq 7$, is tolerant enough to trigger the physics events[1]. Moreover, it rejects proton beam-gas backgrounds. The BPC timing for those events would be 20ns earlier than physics events because BPC sits about 3m downstream of the interaction point.

The efficiency of the BPC trigger (6.1) is investigated using the event sample obtained with a trigger which is independent of (6.1). The trigger bit used in this study requires that at least one of four electron finders should find a positron candidate in CAL. In spite of the requirement, a lot of fake candidates are also triggered in addition to true scattered positrons. The part of those events have positron candidates in BPC. The trigger efficiency, ϵ, is defined as

$$\epsilon = \frac{A \cap B}{A} \tag{6.2}$$

where the group A contains the events satisfying the BPC positron criteria[2] except for the energy requirement and the group B includes the events firing the BPC trigger bit (6.1). In Fig. 6.2, the efficiency is shown as a function of the BPC energy. The efficiency of the first level trigger turns out to be almost 100% at the energy above 7GeV.

6.2.2 Summary of Second and Third level trigger

At the second level trigger, events with $x_l > 5.18$cm were triggered. The x_l is the horizontal position calculated in (5.4). This geometrical cut reduced large amounts of beam-gas backgrounds hitting the inner side of BPC. Finally, at the third level trigger, we required (i) the BPC timing should be within 5ns with respect to the expected physics timing, (ii) $y_{JB} > 0.02$ and (iii) δ should be larger than a threshold value, which was increased from 10 to 25GeV

[1] The input signal for the TDC is generated by a discrimination with a threshold of about 1 GeV. The TDC output becomes 0 if the raw signal is below the threshold.

[2] The BPC positron criteria are defined in Section 6.3.1.

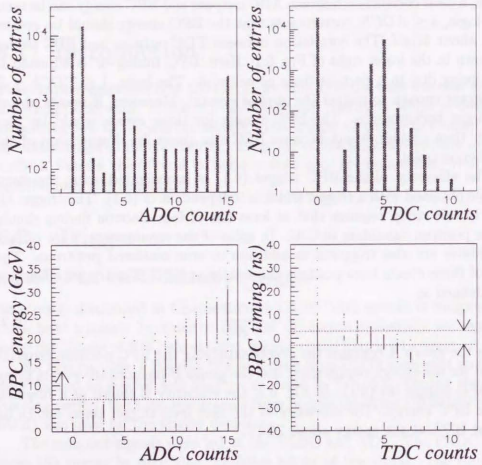

Fig. 6.1: The quantities for trigger decision. The upper left figure is the distribution of ADC counts and the correlation with BPC energy is shown in the lower figure. The upper right figure is of TDC counts and the correlation with BPC timing is in the lower figure. The dotted lines and arrows indicate the offline selection criteria.

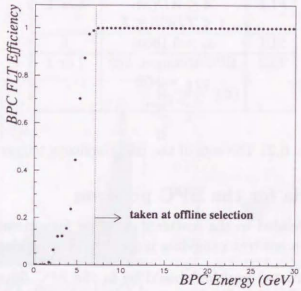

Fig. 6.2: The efficiency of BPC FLT as a function of BPC energy.

during the data taking period. At this stage, y_{JB} and δ were reconstructed using only CAL cells before the noise suppression. The set of cuts at each trigger level is summarized in Tab. 6.2.

Since the trigger rate is sensitive to the beam condition, the trigger need to be prescaled to reduce the rate for the part of the data taking period. They were changed from run to run. In the right column of the Tab. 6.2, the prescale factor for each level is also listed. Taking into account the prescale factors of each run, the integrated luminosity can be calculated as

$$L = \sum_{i=run} l_i \cdot p_i^{FLT} \cdot p_i^{SLT} \cdot p_i^{TLT} \tag{6.3}$$

where p_i^{FLT}=1,1/4, p_i^{SLT}=1 and p_i^{TLT}=1,1/2. The l_i denotes the integrated luminosity for the i-th run. During the 1996 data taking period, the integrated luminosity for this study amounts to 2.433 pb^{-1} in total.

6.3 Offline event selection

The offline event selection is classified into two categories; one is for the positron in BPC and the other is for the hadronic final state.

	requirement	prescale
FLT	$4 \leq ADCh$ $1 \leq TDCh \leq 7$	4 or 1
SLT	$x_l > 5.18$cm	1
TLT	BPC timing $\pm$ 5ns $y_{JB} > 0.02$ $\delta > \delta_{min}$	2 or 1

Tab. 6.2: The sets of the BPC inclusive trigger.

6.3.1 Criteria for the BPC positron

If the quantities related to the scattered positron measurement satisfy the following criteria, a positron candidate is considered to be identified in BPC.

- The reconstructed position should be in the BPC fiducial volume illustrated in Fig. 5.1. Using x_p and y_p in (5.11), the fiducial volume is defined as follows.

$$(5.18 \leq x_p \leq 9.98) \cap (-2.83 \leq y_p \leq 3.17)$$
$$\cap (y_p \leq 11.55 - x_p) \cap (y_p \geq -11.21 + x_p) \tag{6.4}$$

  Fig. 6.3 shows various distributions (open histograms) of the events in the BPC fiducial volume.

- The BPC energy should be greater than 7 GeV. The shaded histogram in Fig. 6.3(a) is the energy distribution after applying all the criteria except the energy requirement.

- Since an electromagnetic shower in BPC is expected to be narrower than a hadronic shower, the σ_x and σ_y obtained from (5.7) and (5.8) should be less than 7mm to remove remaining hadrons. See Fig. 6.3(b).

- The distribution of the BPC timing is shown in Fig. 6.3(c). In order to reject remaining proton beam-gas backgrounds, the BPC timing should be within 3ns with respect to the expected physics timing.

In this thesis, the events satisfying the above criteria are named 'BPC tagged events'.

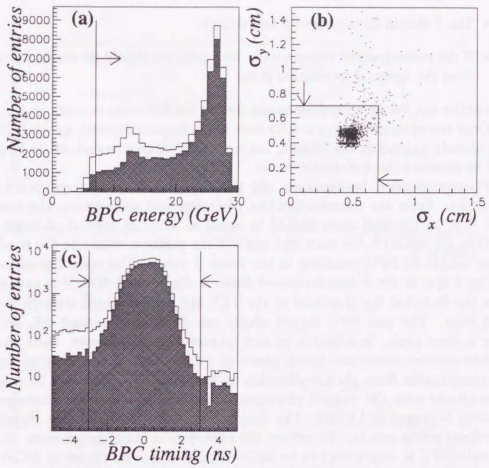

Fig. 6.3: The distributions of the events in the BPC fiducial volume: (a)the BPC energy distributions. The shaded histogram is the one after the BPC positron criteria except the energy requirement. (b)the correlation of σ_x and σ_y. (c)the BPC timing distributions. The shaded histogram shows the distribution after the criteria except the timing requirement. The selection criteria are shown as arrows.

6.3.2 Criteria for the hadronic final state

Furthermore, the following three selection cuts are applied to the BPC tagged events.

- The y_{JB} should be greater than 0.05.
- The δ should be between 35 and 65GeV.
- If the reconstructed vertex exists, its z position should be within 50cm from the nominal interaction point.

The above cut values were determined due to the following reasons.

Only the events with $y_{JB} > 0.05$ were taken because the cut, $y_{JB} > 0.02$, was already applied in the trigger. Later the cut value is varied ± 0.01 from 0.05 to estimate the systematic errors.

Photoproduction backgrounds and radiative events can be reduced by the δ cut. From the conservation law of energy and momentum, the sum of $E - p_z$ in the final state should be equal to $2E_e$. In case of photoproduction, $Q^2 \simeq 0\text{GeV}^2$, the scattered angle of the positron would be too small to be tagged in BPC resulting in the lower δ value. The open histogram in Fig. 6.4(a) is the δ distribution of data. A dip around 20GeV is caused from the fact that the threshold at the TLT had been changed through the 1996 runs. The real BPC tagged events are distributed around $2E_e$ and show a clear peak. In addition to such physics events, however, there can be seen another structure, which grows as δ decreases. It is recognized as the contribution from photoproduction backgrounds[72]. That can be seen more clearly with the 'tagged photoproduction events' where the scattered positron is tagged in LUMIE. The dots in Fig. 6.4(a) represent the tagged photoproduction events. To reduce the photoproduction backgrounds, the cut value of δ is determined to be 35GeV. Later it will be raised to 40GeV to check the sensitivity of remaining backgrounds to the final results.

Finally Fig 6.4(b) is the distribution of the z vertex position which is reconstructed using CTD tracks event by event. At the position of ± 70cm, there are secondary peaks. They arise from so called satellite bunches [3] in the proton beam. In this analysis, only the events whose CTD vertex is found within ± 50cm along the beam line from the interaction point are selected. As described in Section 5.3.4, if the vertex fails to be found, the mean value of -3.3 cm is regarded as the vertex position and such event passes the selection criteria. This is why a spike can be seen at the center

[3] Since the frequency of the RF cavity is 208MHz, part of the beam protons are spilt out and form the additional bunches at $\pm\sim 140$cm.

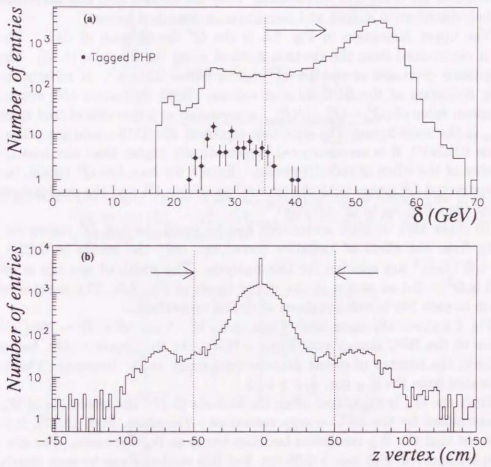

Fig. 6.4: (a)The δ distribution. The dots represent the tagged photoproduction backgrounds. (b) The distribution of z vertex position.

of Fig. 6.4(b). The analysis procedure will be repeated after requiring the existence of CTD vertex as a systematic check in Chapter 8.

6.4 Q^2 and W bin selection

After the above event selections, the fiducial regions in Q^2 and W to be investigated are defined in this section. They are divided into bins according to their distribution shapes and resolution as described below.

The upper histogram in Fig. 6.5 is the Q^2 distribution of data. The Q^2_{el} is determined from the electron method using the formula, (5.16). The acceptance decreases in the low Q^2 region, below 0.2GeV^2. It reflects the inner boundary of the BPC fiducial volume. With diffractive MC events, the mean value of $(Q^2_{el} - Q^2_{true})/Q^2_{true}$ is presented as a function of true value Q^2_{true} in the lower figure. The error bars represent the RMS resolution values. Below 0.2GeV^2, it is reconstructed systematically higher than the true Q^2 because of the effect of radiative events. Except for such low Q^2 region, the reconstructed Q^2 agrees with the true values within 1% and the resolution is better than 10% up to $Q^2 \simeq$0.7GeV^2.

To make sure of high acceptance and to avoid the low Q^2 region suffering from the effect of radiative correction, only the events in $0.22 < Q^2 < 0.7\,\mathrm{GeV}^2$ are selected for this analysis. The width of one bin is set to $\Delta \ln Q^2 = 0.4$ as shown in the upper figure of Fig. 6.5. The number of events in each bin is well equalized with this separation.

Fig. 6.6 shows the same kind of figures for W. A cut-off at $W \sim 260\,\mathrm{GeV}$ is due to the BPC energy cut, E_{BPC} >7GeV. At the opposite side, below 100GeV, the number of events decreases gradually as W decreases. This is originated from the y_{JB} cut, $y_{JB} > 0.05$.

Since the W_{el} is calculated using the formula (5.17), the resolution of W_{el} is determined by the BPC energy resolution. Therefore, from (5.17), it is expected that the W_{el} resolution becomes worse as W_{el} decreases. The situation is improved with $y_{JB} > 0.05$ cut, but this tendency can be seen clearly in the lower figure of Fig. 6.6. The RMS resolution of $(W_{el} - W_{true})/W_{true}$ becomes as poor as 20% around 100GeV. That gives strict constraint to the W bin selection. Starting from 90GeV, the width of the first 3 bins are set to 30GeV which is smaller than 1σ of $(W_{el} - W_{true})/W_{true}$. Above 180GeV where the resolution is good enough, the bin width is set to 20GeV as shown in the upper figure of Fig. 6.6.

Fig. 6.7 shows the scatter plot of the W_{el} and Q^2_{el} The division of the selected bins are also drawn. In the next chapter, the diffractive contribution will be extracted in those 12 bins separately.

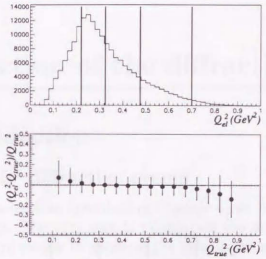

Fig. 6.5: The upper figure is the Q^2_{el} distribution of data. The lower figure shows $(Q^2_{el} - Q^2_{true})/Q^2_{true}$ as a function of Q^2_{true}. Error bars represent the resolution of Q^2.

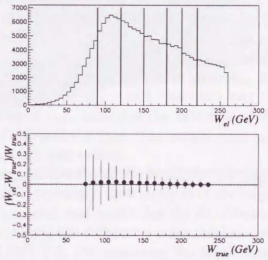

Fig. 6.6: The upper figure is the W_{el} distribution of data. The lower figure shows $(W_{el} - W_{true})/W_{true}$ as a function of W_{true}. Error bars represent the resolution of W.

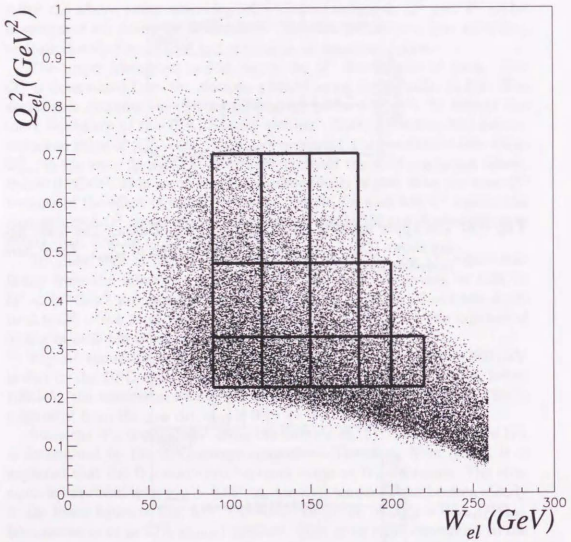

Fig. 6.7: A scatter plot of W_{el} vs Q^2_{el}. The areas divided by lines are selected bins for extracting the diffractive cross section.

7. Extraction of the diffractive events

7.1 Introduction

7.1.1 Low Q^2 diffractive events

After the event selections described in Chapter 6, we have collected low Q^2 events inclusively. The next step is to separate the diffractive events from the non-diffractive events to measure the cross section. The separation is done with the mass distribution in the main detector M_X^{meas}.

In the upper half of Fig. 7.1, there are M_X^{meas} distributions in the Q^2 and W bins specified in Section 6.4. The M_X^{meas} is calculated using the formula (5.18). A distinctive structure can be seen in all bins, a sharp spike at low M_X^{meas} and a broad peak at high M_X^{meas} which moves upward as W increases. In the diffractive process, $\gamma^* + p \rightarrow X + N$, both hadronic system, X and N, are thought to have low mass compared with the total hadronic mass W. The forward going system N with limited mass and p_t would easily escape in the beam pipe as quantitatively studied in Section 7.7.2. Therefore, the observed M_X^{meas} is mainly from the M_X system in the diffractive process.

Fig. 7.2 is the η_{max} distribution. The η_{max} is defined as the maximum pseudorapidity among energy flow objects in an event. Besides the clear peak at the forward detector edge, η_{max} ~3.5, there is a long tail towards the small η_{max} region. The small η_{max} indicates the existence of the large rapidity gap which is a sign of diffractive events. The events with η_{max} <1.5 are referred to as the large rapidity gap events.

In Fig. 7.1, the contribution of the large rapidity gap events are shown as shaded histograms. Apparently, they imply that the large rapidity gap events lie on the low M_X region and determine the distribution shapes there. According to Regge theory, the diffractive cross section, $d\sigma^{diff}_{\gamma^* p}/dM_X^2$, is mainly proportional to $1/M_X^2$ [15, 16], assuming the triple Regge limit[8]. That is the reason why the large rapidity gap events appeared rather flat in the $\ln(M_X^{meas})^2$ distributions as seen in the lower half of Fig. 7.1.

In Fig. 7.3 and Fig. 7.4, event displays of the low Q^2 events are presented. Fig. 7.3 is an example of the non-diffractive events. The large amounts of energy deposits in FCAL can be seen around the forward beam pipe. Fig. 7.4

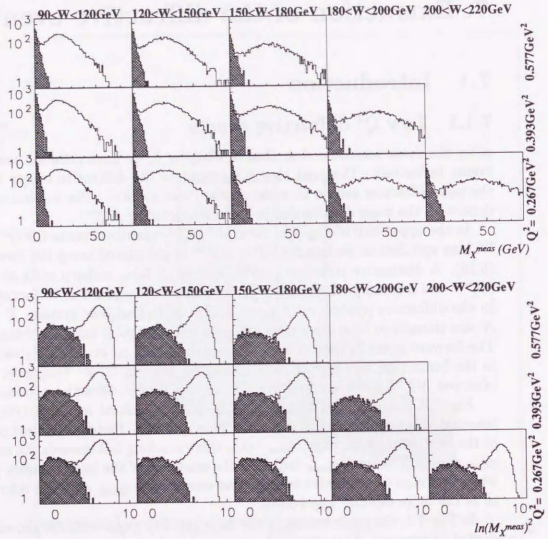

Fig. 7.1: The M_X^{meas} distributions. The corresponding W and Q^2 values are labeled at the top and right side of the figures. The shaded histograms show the large rapidity gap events, η_{max} <1.5. The lower half of figures are $\ln(M_X^{meas})^2$ distributions.

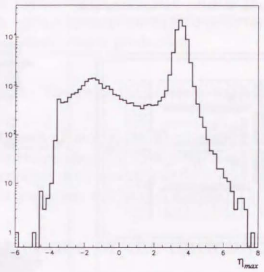

Fig. 7.2: The η_{max} distribution.

is an example of the large rapidity gap events. It shows the large rapidity space filled with no detector activities in the forward region.

7.1.2 Overview of the analysis procedure

This chapter is devoted to describing how the non-diffractive contribution is subtracted in order to extract the number of diffractive events, which will be unfolded to the produced number of events in Chapter 8. Prior to the complete description of the analysis, it is outlined briefly in this section.

At first, it is demonstrated that the final state seen in the data can be reproduced well by the mixture of MC events. The diffractive MC events are used for the M_X correction and the unfolding. As mentioned at the end of Chapter 5, the M_X^{meas} obtained from (5.18) is still imperfect. By comparing the M_X^{meas} and the true M_X using MC events, the correction factor is obtained as a function of the M_X^{meas}.

With corrected $\ln M_X^2$ distributions, the non-diffractive contribution is subtracted by means of a fitting procedure with an exponential function. The method takes advantage of the difference of $\ln M_X^2$ shapes between the diffractive and non-diffractive events. Before applying it to the data, the method is tested using MC events in order to demonstrate the validity of the method. Then it is applied to the data and we extract the number of

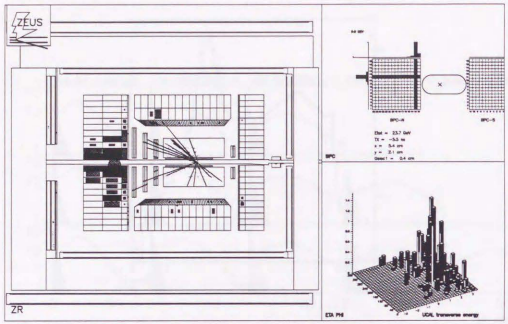

Fig. 7.3: An example of the non-diffractive events.

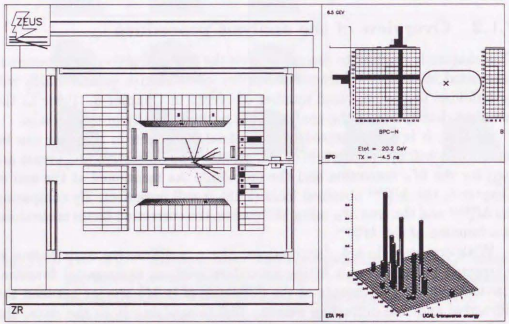

Fig. 7.4: An example of the large rapidity gap events.

A	non-diffractive
B	single photon dissociation from $I\!P I\!P I\!P$ term, $\propto 1/M_X^2$
C	single photon dissociation from $I\!P I\!P I\!R$ term, $\propto 1/M_X^3$
D	elastic vector meson production

Tab. 7.1: The generated processes using EPSOFT

diffractive events in each Q^2 and W bin. Further the reliability of the method is checked using the events tagged by Proton Remnant Tagger (PRT) because those events are enriched with non-diffractive events. Finally, the effect of the proton dissociative events will be also discussed.

7.2 Comparisons of the data and MC

In this section, we show that the M_X^{meas} distribution is well reproduced with the sum of various MC events.

The EPSOFT has the ability to generate various kinds of processes as described in Chapter 4. However, the observed hadronic final state cannot be described by any single process; plural number of processes should be mixed with proper fractions to reproduce the data. The four processes summarized in Tab. 7.1 are used for the comparison. The process A is the non-diffractive contribution. Two different types of single photon dissociative processes are prepared to account for the shape of $\ln(M_X^{meas})^2$ distribution. In process B, all three trajectories are Pomerons ($I\!P I\!P I\!P$) and the cross section, $d\sigma/dM_X^2$, is almost proportional to $1/M_X^2$. In process C, one of the trajectories is a Reggeon and others are Pomerons ($I\!P I\!P I\!R$) and the M_X dependence of $d\sigma/dM_X^2$ is steeper, $\propto 1/M_X^3$. The process D is the elastic vector meson production.

In order to obtain the $\alpha_{I\!P}(0)$ from the W dependence of the diffractive cross section, we need to select the single photon dissociative events (B and C) and the other contribution should be subtracted. The biggest contribution is from non-diffractive events and it will be subtracted by fitting $\ln M_X^2$ distributions to a certain function. The contribution from the proton dissociative diffraction will be also discussed later.

In Fig 7.5, the $\ln(M_X^{meas})^2$ distributions of different processes are overlaid with that of data. The non-diffractive process (A) is enhanced at high M_X^{meas}. The $I\!P I\!P I\!P$ term (B) show rather flat distribution. The $I\!P I\!P I\!R$ term (C) show a decreasing distribution and characterizes the hump seen at $\ln(M_X^{meas})^2 \sim 1$. The elastic vector meson production (D) exhibits a strong

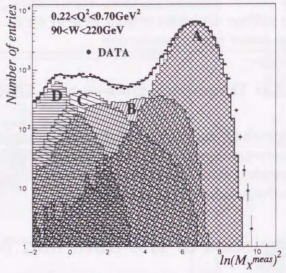

Fig. 7.5: The $\ln(M_X^{meas})^2$ distributions of the data and MC.

peak at $\ln(M_X^{meas})^2 \sim -0.5$, corresponding to the mass of ρ^0 meson. The fractions of them to be mixed are determined by minimizing the χ^2 defined as

$$\chi^2 = \frac{1}{(n_{bins}-3)} \sum_{bins} \frac{(N_{data} - \sum_i \alpha_i N_i)^2}{(N_{data} - \sum_i \alpha_i^2 N_i^2)} \tag{7.1}$$

where i denotes the process ID listed in Tab. 7.1, N means the number of events in a bin, n_{bin} is the number of bins used for the fit, and α_i is the fraction of the each process. The total number of MC events were fixed to the total number of events in data by giving the constraint,

$$\sum_{bins} N_{data} = \sum_{bins} \sum_i \alpha_i N_i. \tag{7.2}$$

In Fig. 7.5, the four processes are plotted according to the weights obtained from the fit. The sum of them are also shown as an open histogram. As seen in Fig. 7.5, the mixture of MCs describe the $\ln(M_X^{meas})^2$ distribution of the data well.

The other quantities of the events are compared with MC using the obtained fraction. The top two figures in Fig. 7.6 are the Q^2 and W distributions. Open histograms are the sum of four MC events and hatched ones show the diffractive contributions, $B+C+D$. The distributions of MC show good agreements with those of the data presented as dots. The other four

distributions shown in the figure are the total energy of objects, δ, y_{JB} and z vertex position. From those figures, it is concluded that the mixed MC events reproduce the data reasonably well.

7.3 The M_X measurement

7.3.1 The M_X measurement and acceptance limit

In Section 5.4.3 and Appendix D, the clustering algorithm into energy flow objects was described. From four momenta of the objects, the M_X^{meas} is calculated using the formula (5.18). The correspondence between the M_X^{meas} and the mass of photon dissociated system M_X^{true} is studied with single photon dissociative MC events. As shown in Fig. 7.7, there is a good correlation between them but the M_X^{meas} tends to be smaller than the M_X^{true}. There are two reasons to be considered. One of them is inactive material in front of CAL and the other is limits of CAL acceptance. As M_X increases, particles tend to be emitted to wider rapidity region. Then the number of particles going very forward would be increased and the acceptance effect becomes more and more crucial. Fig. 7.8 is shown to demonstrate the effect. The solid histograms are the distributions of $\ln(M_X^{true})^2$, which are almost flat because the $I\!P I\!P I\!P$ MC is used here. The $\ln(M_X^{meas})^2$ are shown as dots in the figures. At high M_X, the flat distributions are distorted due to the effect of the acceptance limits. The broken histograms show the $\ln(M_X^{acc})^2$, which is similar to $\ln(M_X^{true})^2$ but the particles whose emitted angle is lower than our detector acceptance is excluded. It turns out that the M_X^{meas} reproduces the M_X^{acc} fairly well. That is, the flat distributions are already distorted at this level. Thus the acceptance limits restrict the M_X measurement dominantly. In subsequent sections, two methods are introduced to correct the M_X^{meas}.

7.3.2 The M_X correction method A

In this section, the ratio of the M_X^{meas} to the M_X^{true},

$$f(Q^2, W, M_X) = \frac{M_X^{meas}}{M_X^{true}} \tag{7.3}$$

is investigated with diffractive MC events. The ratio can be regarded as a correction factor and the M_X^{meas} is corrected as

$$M_X^{corr} = \frac{M_X^{meas}}{f} \tag{7.4}$$

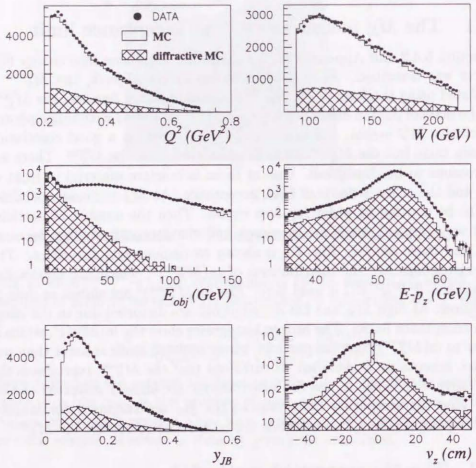

Fig. 7.6: The comparisons of the data and MC. Open histograms are the sum of four MCs, and hatched ones show the diffractive contributions. The data are represented as dots. The top two figures are the Q^2 and W distributions, and rest of the figures are distributions of the hadroninc final states.

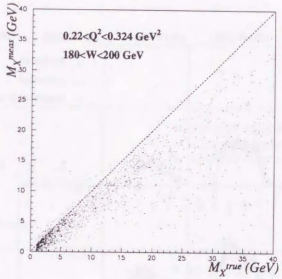

Fig. 7.7: The correlation between the M_X^{true} and M_X^{meas}.

using the correction factor. The factor is a function of all the relevant kinematic variables, for example Q^2, W and M_X, as indicated explicitly in (7.3).

In Fig. 7.9, the Q^2, W and M_X dependence is examined as a function of the M_X^{meas}. As mentioned in Chapter 4, EPSOFT generates only the events with $M_X \geq$1GeV for the single photon dissociative processes. This makes it difficult to obtain reliable correction factors at low M_X region. Therefore, the correction factors are obtained using the events with $M_X^{meas} \geq$2GeV.

Fig. 7.9(a) shows the ratio of the M_X^{meas} to the M_X^{true} for different Q^2 regions. Little Q^2 dependence is observed. Fig. 7.9(b) shows the ratio for different W regions. If the M_X^{meas} is high, the ratio tends to become larger as W decreases. However, little W dependence is observed at M_X^{meas} <15GeV where we are going to extract the diffractive cross section. From these observations, the Q^2 and W dependence is neglected and only the M_X dependence is considered hereafter.

Fig. 7.9(c) shows the ratio after combining all the Q^2 and W bins. From the figure, the M_X^{meas} reproduces almost 90% of the M_X^{true} around 3GeV. As M_X^{meas} increases, it decreases rapidly to 70% and becomes almost constant. It is fitted to a function of the form,

$$f(M_X^{meas}) = p_1 \cdot \exp(-p_2 \cdot M_X^{meas}) + p_3 \tag{7.5}$$

where p_1, p_2 and p_3 are free parameters. The result of the fit is summarized

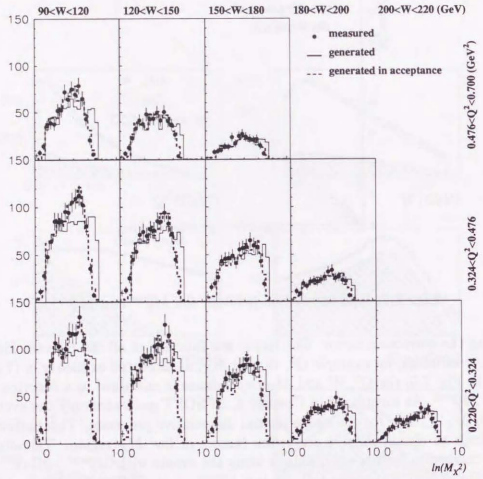

Fig. 7.8: The $\ln M_X^2$ distributions of the $I\!P I\!P I\!P$ events. The solid and broken histograms are for the M_X^{true} and M_X^{acc}, respectively. The M_X^{meas} are also shown as dots.

p_1	0.4161±0.0158
p_2	0.2281±0.0122
p_3	0.7190±0.0034

Tab. 7.2: The result of the fit for the M_X correction factor.

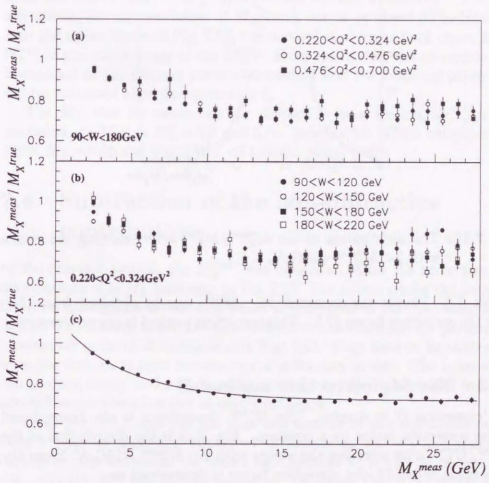

Fig. 7.9: The ratio of the M_X^{meas} to the M_X^{true} for (a)different Q^2 and (b)different W regions. In figure(c), all the Q^2 and W bins are combined and the ratio is fitted to a function of the form (7.5) in the text.

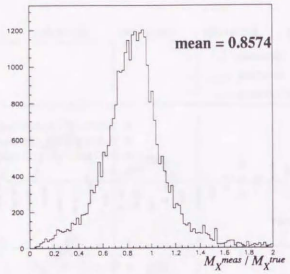

Fig. 7.10: The distribution of the M_X^{meas}/M_X^{true} after selecting the events with $2< M_X^{meas} <15$GeV.

in Tab. 7.2. Finally the corrected M_X, M_X^{corr}, can be obtained from (7.4) using the correction factor (7.5). This correction method is named 'correction A'.

7.3.3 The M_X correction method B

The 'correction B' is simpler. The M_X^{meas} dependence is also ignored and let the correction factor be a constant. Fig. 7.10 is the distribution of the M_X^{meas}/M_X^{true} after selecting the events with $2< M_X^{meas} <15$GeV. From the mean value of 0.8574, the correction factor is determined as

$$f = 0.8574 \tag{7.6}$$

in the correction B.

7.3.4 Comparison of correction methods

Fig. 7.11 shows the distributions of $\ln(M_X^{true})^2$ and $\ln(M_X^{corr})^2$. The closed and open circles represent the results from the correction methods A and B, respectively. Compared with the M_X^{meas} seen in Fig. 7.8, it can be seen that the M_X^{corr} describes the M_X^{true} much better. The correction B, simply

multiplying a constant, only shifts $\ln M_X^2$ distributions without changing their shapes. On the other hand, the correction A in which the correction factor varies as M_X^{meas} transforms the shapes of distributions and results in fitting to the shapes of $\ln(M_X^{true})^2$ better than after the correction B. The difference between the two methods also can be seen in Fig. 7.12 which shows the mean and rms of $(M_X^{corr} - M_X^{true})/M_X^{true}$ as a function of the M_X^{true}. For both corrections, the rms resolution of M_X turns out to be about 30%. However, from the upper figure of Fig. 7.12, the method A corrects back closer to the M_X^{true} in the whole range of the M_X^{true}. From this result, the correction A is determined as the primary correction method and the following procedures will be continued after the correction A.

The M_X bins for measuring the diffractive cross section, $d\sigma_{\gamma^* p}^{diff}/dM_X$, are chosen as $2.2< \ln M_X^2 <3.6$ and $3.6< \ln M_X^2 <5.0$, which correspond to $3.00< M_X <6.05$ and $6.05< M_X <12.2$GeV, respectively.

7.4 Subtraction of the non-diffractive contribution

In the previous section, the M_X^{meas} was corrected. After the correction, the distributions of $\ln M_X^2$ were seen in Fig. 7.13. The points are for the data and the solid histograms are for MC which is composed of four processes listed in Tab. 7.1. Among them, the non-diffractive contributions are particularly represented as hatched histograms in Fig. 7.13. They have to be subtracted from the data to extract the number of diffractive events. The subtraction can be done owing to the characteristics of the $\ln M_X^2$ distributions from the non-diffractive contributions as described below.

From Fig. 7.13, one can see that the number of non-diffractive events form a peak at high M_X ($\ln M_X^2$=7~8 depending on W) and decreases rapidly as M_X decreases. As shown in Appendix E, it can be proved that $dN_{nondiff}/d\ln M_X^2$ falls off exponentially. Therefore, the $\ln M_X^2$ distribution observed in the data is expected to be formulated to

$$\frac{dN}{d\ln M_X^2} = D + c\cdot\exp(b\cdot\ln M_X^2) \tag{7.7}$$

where D denotes the diffractive contribution.

Further the D can be decomposed into three terms:

$$D = d_{ppp} + d_{ppr} + d_{vm}. \tag{7.8}$$

The contribution from $I\!P I\!P I\!P$ process, d_{ppp}, is expected to be almost constant because the cross section behaves like $\propto 1/M_X^2$. On the other hand, the cross

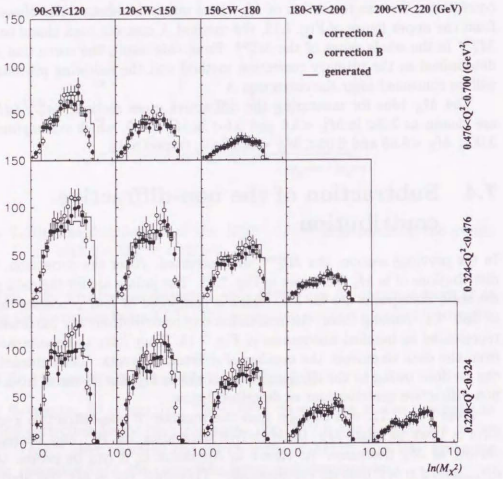

Fig. 7.11: The $\ln M_X^2$ distributions of the $I\!P I\!P I\!P$ events. The closed and open circles are the results from the M_X correction methods A and B, respectively. The M_X^{ture} is also shown as histograms.

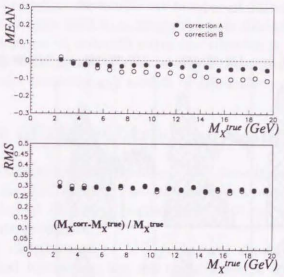

Fig. 7.12: The mean and rms of $(M_X^{corr} - M_X^{true})/M_X^{true}$ as a function of the M_X^{true}.

section of $I\!P I\!P I\!R$ term is proportional to $1/M_X^3$, then d_{ppr} is expected to be $\propto \exp(-\frac{1}{2}\ln M_X^2)$.

As long as the higher $\ln M_X^2$ region is concerned, the contribution from $I\!P I\!P I\!R$ can be neglected and D can be regarded as a constant parameter. Therefore, the lower limit for the fit is determined to be 3.3. The upper limits for the fit are determined from the data. The same upper limits are used for the same W bins. The regions to be fitted are summarized in Tab. 7.3 and drawn in Fig. 7.13 by dotted lines.

From the results of the fits, the non-diffractive contribution is subtracted

W (GeV)	lower limit	upper limit
90 - 120	3.3	5.9
120 - 150	3.3	6.5
150 - 180	3.3	6.9
180 - 200	3.3	7.1
200 - 220	3.3	7.3

Tab. 7.3: The $\ln M_X^2$ regions to be fitted to the form (7.7).

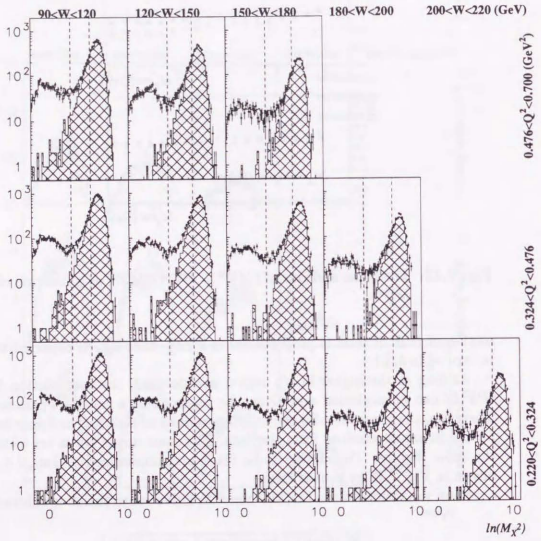

Fig. 7.13: The $\ln M_X^2$ distributions after the M_X correction method A. The points are for data the solid histograms are for the sum of four MC processes. Particularly, the non-diffractive process is represented as hatched histograms. The regions to be fitted to (7.7) are indicated by dotted lines.

statistically to extract the number of diffractive events. Note that the parameter D is not used to determine the number of diffractive events, but the parameters b and c are used to subtract the non-diffractive contribution. In this way, the amount of non-diffractive contribution is determined directly from the $\ln M_X^2$ distributions of the data and the diffractive contribution is extracted without assuming any models of diffractive processes.

7.5 Test of the subtraction using MC

This section demonstrates the validity of the non-diffractive subtraction by applying it to the MC events. The method is examined by checking if the extracted number of diffractive events agrees with the number of generated diffractive events as follows.

The $\ln M_X^2$ distributions of MC events are shown again in Fig 7.14. Overlaid hatched histograms are the non-diffractive components. The fit to the form (7.7) is applied to the $\ln M_X^2$ distributions in each Q^2 and W bin. The results are shown as solid curves in Fig 7.14. In addition, the non-diffractive exponential slopes are also shown as the solid lines. The closed circles in Fig 7.15 are the obtained value of parameter b as a function of W in each Q^2 region. They are distributed around $b \sim 1.4$ and little Q^2 and W dependence can be seen.

As a check, the $\ln M_X^2$ distributions of non-diffractive MC events are solely fitted to the form (7.7) with D =0. The resulted exponential functions are drawn as dotted lines in Fig 7.14. As seen in the figure, the solid and dotted lines are close to each other in most of the Q^2 and W regions. It demonstrates that the method brings out the non-diffractive contribution adequately. The slope parameters from the non-diffractive MC events are also shown as open circles in Fig 7.15 for comparisons. From Fig 7.15, it turns out again that the non-diffractive backgrounds are well reproduced by the results of the fits.

Up to now, in the fitting procedure, there are three free parameters, D, c and b for each bin. However, since there is little difference in the slope parameter b for all Q^2 and W bins, a common slope will be used. In order to determine the slope, the fit is done again using only higher W bins. The selected bins are surrounded by the thick frame in Fig 7.14. The higher W bins are chosen because larger region of the $\ln M_X^2$ can be taken for the fit. As a result, the nominal slope b_{nom} is obtained as 1.41 ± 0.04.

Finally, fixing the b to the nominal value, the $\ln M_X^2$ distributions are fitted to the form (7.7). Then the non-diffractive contribution is subtracted according to the results of the fits. In Fig 7.16, the numbers of events after the subtraction are shown as closed circles. As seen in the figure, they are

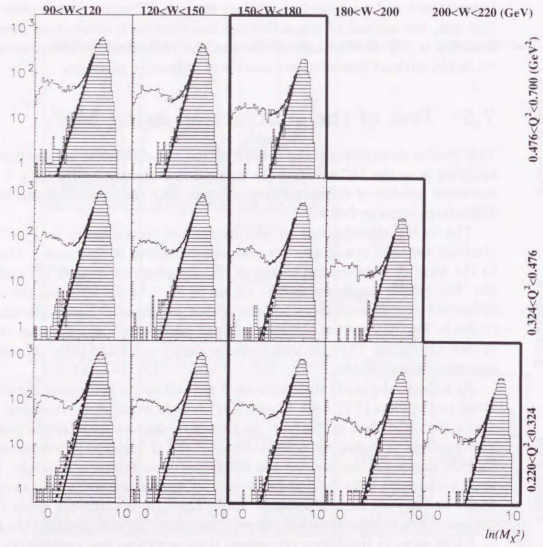

Fig. 7.14: The $\ln M_X^2$ distributions of MC events. The open histograms are the sum of four different processes and the hatched ones are the non-diffractive components. The results of the fit to the form (7.7) are drawn as solid curves along the histograms. The exponential parts are also shown as solid lines which should be compared with the dotted lines obtained from the pure non-diffractive MC events. The bins surrounded by the thick frame are used for the determination of the nominal slope.

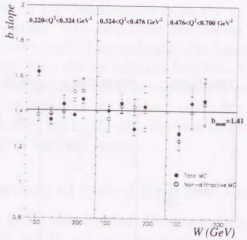

Fig. 7.15: The b slope as a function of W for each Q^2 region. The closed and open circles are obtained from the summed and non-diffractive MC events, respectively.

consistent with the numbers of diffractive events (open circles) in the whole Q^2, W and M_X ranges. Thus the number of diffractive events is extracted successfully in the case of the MC events.

7.6 Extraction of the diffractive events

7.6.1 Subtraction of beam-gas backgrounds

Finally, we extract the number of diffractive events in the data by applying the non-diffractive subtraction method that turned out to work fine in the case of the MC. However, in addition to the physics events resulting from the *ep* collisions, the backgrounds from the interaction of the beam particle and the residual gas in the beam pipe are contaminated in the data sample. There are two types of such backgrounds, electron beam-gas backgrounds and proton beam-gas backgrounds. They must be subtracted before the fitting and unfolding procedures.

In total, 220 bunches are supplied by HERA. They are composed not only of the *ep* collision bunches but also of the positron or proton unpaired bunches. The positron(proton) unpaired bunches are called electron(proton) pilot bunches and they are used to estimate the amounts of electron(proton)

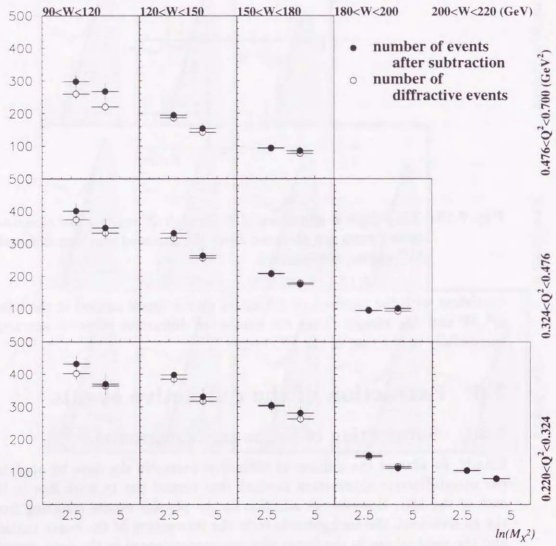

Fig. 7.16: The number of events after the non-diffractive subtraction (closed circles) and the number of diffractive events (open circles).

beam-gas backgrounds.

In Fig. 7.17, the $\ln M_X^2$ distributions from the ep collision bunches are shown as the histograms. The dots show the events from the electron pilot bunches. They are weighted according to the beam currents to compare the number of events from the ep collision bunches. Fig. 7.17 tells that the electron beam-gas backgrounds are contaminated at most 10% but typically about 1%. The contribution of the electron beam-gas backgrounds are subtracted statistically from the $\ln M_X^2$ distributions to apply the non-diffractive subtraction method in the next section.

7.6.2 Subtraction of non-diffractive backgrounds

Fig. 7.18 shows the $\ln M_X^2$ distributions after subtracting the beam-gas backgrounds. In each Q^2 and W bin, the distribution is fitted to the form (7.7). The regions to be fitted are summarized in Tab. 7.3. The curves in Fig. 7.18 show the results of the fits and the solid lines are the obtained non-diffractive contributions.

The values of the b slopes are plotted as closed circles in Fig. 7.19. They are compared with the slopes from MC (open circles) in the figure. Both of them are consistent with each other in most of the bins. The nominal slope is determined from the higher six W bins, which are surrounded with a thick frame in Fig. 7.18. The nominal slope is extracted as 1.39±0.03 and it is consistent with the one from MC, 1.41.

As seen in the upper half of Fig. 7.20, the fitting procedure is repeated with the constraint of $b = b_{nom}$ in (7.7). Then, according to the obtained parameters from the fits, the non-diffractive backgrounds are subtracted statistically. The lower half of Fig. 7.20 shows the $\ln M_X^2$ distributions after the subtraction.

Finally, the measured number of diffractive events, N_{diff}^{meas}, for each Q^2, W and M_X bin is shown in Fig. 7.21 and summarized in Tab. 7.4. In Chapter 8, the N_{diff}^{meas} is unfolded to the produced number of events to calculate the diffractive cross section.

7.7 Cross check of the non-diffractive subtraction

7.7.1 The b-slopes from PRT tagged data

In Section 7.5, the non-diffractive subtraction was tested with the MC events, which describe the data well as seen in Fig. 7.13. In this section, we attempt

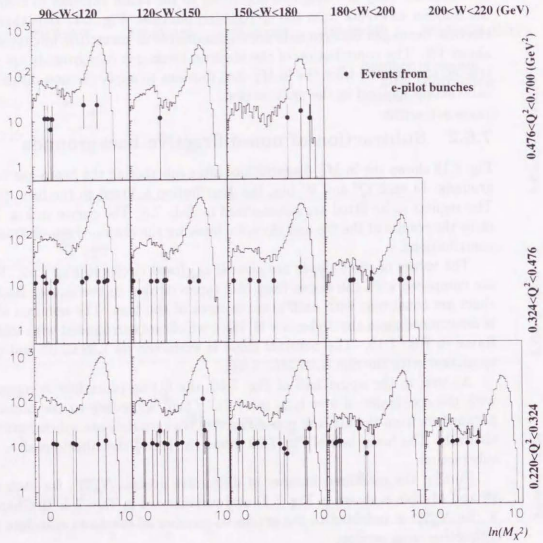

Fig. 7.17: The $\ln M_X^2$ distributions of the events in the *ep* collision bunches. The dots show the contribution from the electron pilot bunches. They are weighted according to the beam currents to be subtracted statistically.

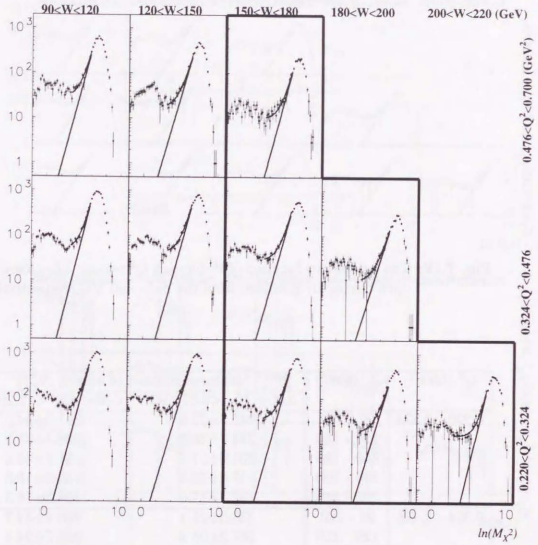

Fig. 7.18: The $\ln M_X^2$ distributions of the data after subtracting the beam-gas backgrounds. The results of the fit to the form (7.7) are drawn as the curves along the histograms. The exponential fall-offs are also shown as the solid lines. The bins surrounded with the thick frame are used to determine the value of the nominal slope, b_{nom}.

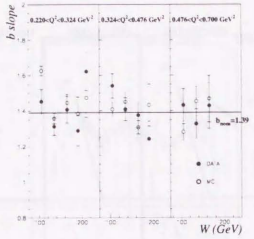

Fig. 7.19: The b slope as a function of W for each Q^2 region. The closed and open circles are obtained from the data and MC, respectively.

Q^2 (GeV^2)	W (GeV)	Measured number of events, N_{diff}^{meas}	
		3.00< M_X <6.05(GeV)	6.05< M_X <12.2(GeV)
0.220 - 0.324	90 - 120	345.7±27.6	311.3±34.0
	120 - 150	344.7±26.3	288.4±33.8
	150 - 180	303.9±21.6	251.1±23.6
	180 - 200	147.0±25.3	136.3±18.3
	200 - 220	122.3±17.0	104.3±16.3
0.324 - 0.476	90 - 120	333.5±21.1	260.1±34.7
	120 - 150	287.2±25.4	268.7±24.4
	150 - 180	237.4±16.0	190.6±21.5
	180 - 200	116.8±11.0	71.95±16.4
0.476 - 0.700	90 - 120	230.7±17.1	175.1±30.2
	120 - 150	149.2±13.2	142.5±17.9
	150 - 180	70.8±8.8	79.9±11.1

Tab. 7.4: The measured number of diffractive events.

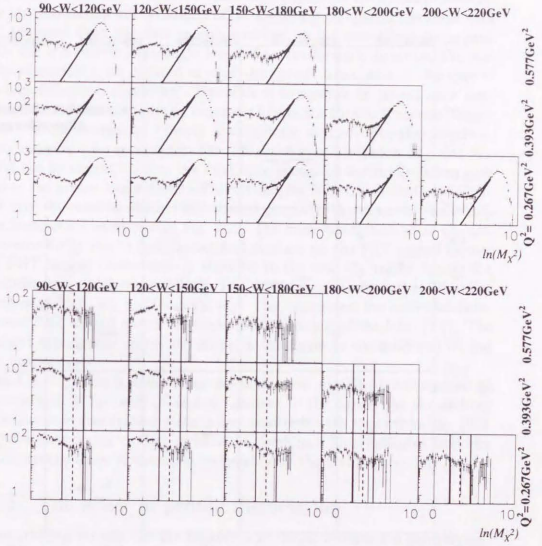

Fig. 7.20: In the upper half, the M_X method is applied to $\ln M_X^2$ distributions with the fixed value of $b = b_{nom}$. According to the results of the fits, non-diffractive backgrounds are subtracted statistically. The $\ln M_X^2$ distributions after the subtraction are seen in the lower half of the figure. The regions between solid lines are used to extract the diffractive cross section. The dotted lines show the bin boundaries.

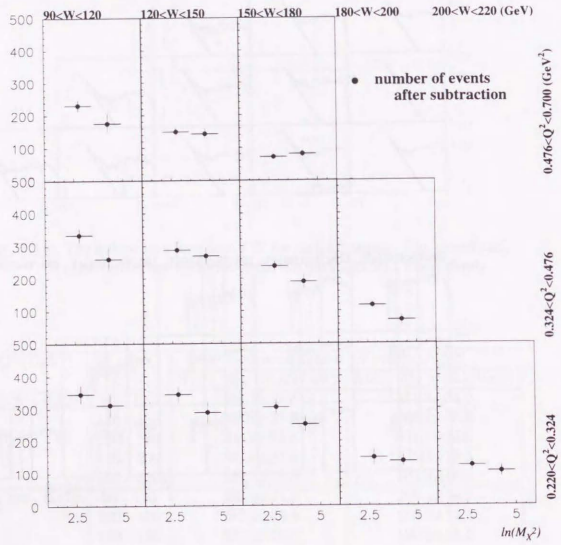

Fig. 7.21: The measured number of events after the non-diffractive subtraction with the nominal slope, $b_{nom} = 1.39$. The exact numbers are summarized in Tab. 7.4.

to examine the method using the real data sample as follows.

For subtracting the non-diffractive contribution properly, it is important to obtain the reasonable value of exponential slope from the fitting procedure. One way to examine the reliability of the method is comparing the slope with that obtained from the data sample enriched by the non-diffractive events. Since the $\gamma^* p$ system is strongly boosted to the forward direction, the majority of particles are emitted around the proton beam axis in the case of $\gamma^* p$ non-diffractive scattering. Therefore it is possible to collect such non-diffractive dominated events by requiring hits in the Proton Remnant Tagger (PRT), which consists of 2 layers of scintillator tiles covering the pseudorapidity range of $4.0 < \eta < 6.0$[42]. The diffractive events with low M_X and M_N would not be tagged because the final state proton or nucleonic system goes close to the proton beam direction and it escapes from the detection of PRT.

Using the runs in which PRT worked properly, the shape of the $\ln M_X^2$ distributions are compared in Fig. 7.22. The open histograms show the distributions for all events and the hatched ones are for the PRT tagged events. The PRT tagged events show a shoulder in the low M_X region beside the non-diffractive exponential fall-off. The shoulder comes from the diffractive events with high M_X and/or high M_N. The histograms for both the inclusive and PRT tagged events are fitted to the function of the form (7.7). The obtained exponential slopes are drawn in the figure as the solid and dotted lines, respectively.

In Fig. 7.23, the b slopes from the both event samples are compared as a function of W for each Q^2 region. As seen in the figure, the slopes from the inclusive events (closed circles) are consistent with those from the PRT tagged events (open circles) in most of the bins. This indicates that the non-diffractive slope is extracted reasonably by the fitting procedure.

7.7.2 The effect of proton dissociation

As an additional check for the reliability of the non-diffractive subtraction, the effect of the proton dissociation is examined in this section.

In Section 7.2, MC events of the different processes in Tab. 7.1 were combined to describe the data. At that time, the proton dissociative diffractive processes were not included. This was due to the uncertainties in their fractions to be combined.

In this section, fraction of the EL and GD MC events are replaced with the PD and DD MC events, respectively (See Fig. 2.2). The fraction of the PD is determined by comparing the PRT tagging rate between the ρ^0 candidates in the data and the EL and PD MC events. The fraction of the DD is determined by comparing the PRT tagging rate between the large

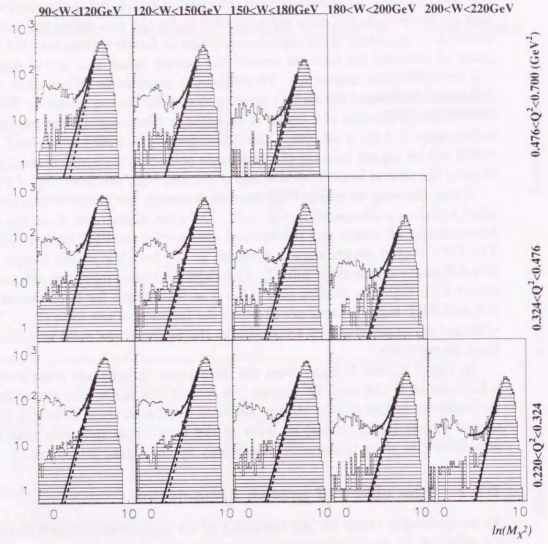

Fig. 7.22: The $\ln M_X^2$ distributions using the runs in which PRT was available. The open and hatched histograms are for the inclusive and PRT tagged events, respectively. The solid and dotted lines show the exponential slopes from the fitting procedure for the inclusive and PRT tagged events, respectively.

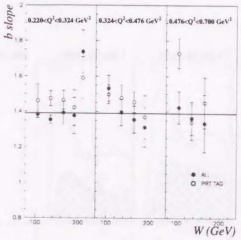

Fig. 7.23: The b slope as a function of W for each Q^2 region. The closed and open circles are obtained from the inclusive and PRT tagged events, respectively.

rapidity gap events in the data and the GD and DD MC events. Then the shapes of $\ln M_X^2$ distributions are slightly changed and they become as seen in Fig. 7.24. The hatched histograms represent the contribution of the proton dissociative diffraction, PD and DD.

When the M_N is low, the particle multiplicity is expected to be small. Then the particles from the proton dissociative system would be well collimated around the direction of the incoming proton. However, as the M_N grows, the number of particles increases and they spread transversely wide enough to be in the acceptance of CAL. As a result, the M_X would be reconstructed much higher than the real M_X because of those particles detected around the FCAL beam pipe region. This is why hatched histograms in Fig. 7.24 show humps at high M_X in spite of the diffractive processes. Those events are gathered at the foot of the non-diffractive exponential slopes and it might cause a shallower b slope.

In order to know how significant they are in this analysis, the fitting procedure is applied to the MC events with the proton dissociation. In Fig. 7.25, the obtained b slopes are compared with the ones from the MC events without the proton dissociation. From the figure, it is not likely that the proton dissociative processes distort the non-diffractive exponential slopes significantly.

Using the above PD and DD MC events, the value of such M_N^{acc} are

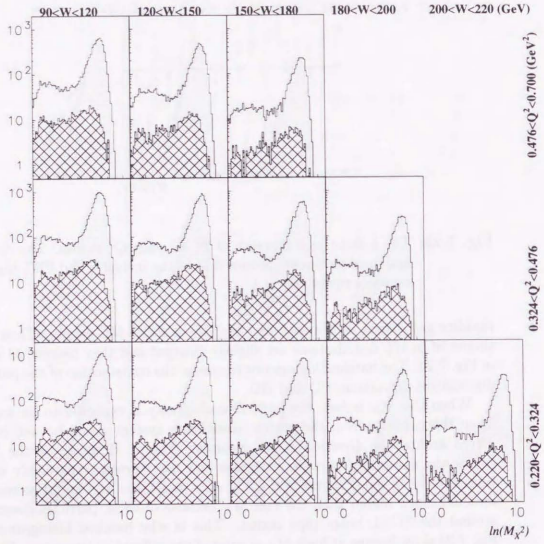

Fig. 7.24: The $\ln M_X^2$ distributions of MC events including the PD and DD processes. Their fractions to be combined are determined according to the PRT tagging rate. The hatched histograms represent the contribution of the proton dissociation, the sum of PD and DD.

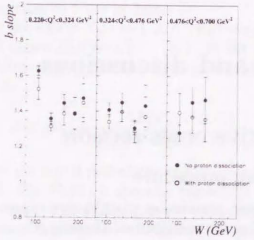

Fig. 7.25: The b slope as a function of W for each Q^2 region. The closed and open circles are obtained from the MC events without and with proton dissociative processes, respectively.

obtained that satisfies (1) the number of events with $M_N < M_N^{acc}$ migrating outside of the investigated M_X bins and (2) the number of events with $M_N > M_N^{acc}$ migrating into the M_X bins are equal to each other. The value of M_N^{acc} is found to be about 6GeV, which is consistent with 5.5±1.5GeV quoted in [23]. From this result, we would say that we measure the diffractive cross section, $\gamma^* + p \to X + N$, with $M_N < 6$GeV.

8. Results and discussions

8.1 Diffractive cross section

8.1.1 Unfolding procedure

In the previous chapter, the number of diffractive events was taken by subtracting the non-diffractive contribution. However, the measured number of events, N_{diff}^{meas}, differs from the produced number of events, N_{diff}^{prod}, because of the following possible reasons.

- The number of events is reduced due to the limited detector acceptance and the inefficiency of the event selections.
- The limited resolution of the kinematic variables causes the migration of events between adjacent bins.
- In the formulae of the electron method, (5.16) and (5.17), the energy of initial state positron is assumed to be the positron beam energy. Therefore the Q^2 and W would be overestimated in case a photon is emitted from the initial state positron.

In order to extract the diffractive cross section, the N_{diff}^{meas} must be unfolded to the N_{diff}^{prod} by taking them into account.

From the mathematical point of view, the relation of the N_{diff}^{prod} of i-th bin and the N_{diff}^{meas} of j-th bin can be written down as

$$N_j^{meas} = \sum_i M_{ji} \cdot N_i^{prod} \tag{8.1}$$

where the matrix element M_{ji} can be obtained from the diffractive MC events. Hence, in principle, the N_{diff}^{prod} could be obtained if the inverse matrix of M was found. However, the matrix M cannot be inverted if it is singular. Even if the inverse matrix exists, it would be possible to result in the negative N_{diff}^{prod}. To avoid such numerical problems, the Bayes unfolding procedure[73] is adopted as described below. Another benefit from the Bayes unfolding is

that the N_{diff}^{prod} can be obtained even if the global event shapes in the MC are not simulated to be close to those in data.

Let us suppose the effects $E_j (j = 1, 2, \ldots, n_E)$ were observed by an experiment from the causes $C_i (i = 1, 2, \ldots, n_I)$. In the Bayes' theorem, the conditional probability of the j-th effect to be produced from the i-th cause, $P(C_i|E_j)$, is given as

$$P(C_i|E_j) = \frac{P(E_j|C_i) \cdot P_0(C_i)}{\sum_{k=1}^{n_I} P(E_j|C_k) \cdot P_0(C_k)} \tag{8.2}$$

where the $P_0(C_i)$ is the initial probability of the cause and it is normalized as $\sum_{i=1}^{n_I} P_0(C_i) = 1$. The $P_0(C_i)$ is given by the MC at the first iteration of the unfolding procedure. The $P(E_j|C_i)$ is the conditional probability of the i-th cause to produce j-th effect and it is determined from the diffractive MC events. The value of ϵ_i defined as

$$\epsilon_i = \sum_{j=1}^{n_E} P(E_j|C_i) \tag{8.3}$$

is the efficiency of the i-th cause to be detected in the observed effects. Using the probability (8.2) and considering the efficiency (8.3), the N_{diff}^{prod} of the i-th bin can be calculated as

$$N_i^{prod} = \frac{1}{\epsilon_i} \cdot \sum_{j=1}^{n_E} P(C_i|E_j) \cdot N_j^{meas} \tag{8.4}$$

from the N_{diff}^{meas}'s in all observed bins. In addition, a new set of initial probabilities of the cause can be calculated as

$$P_0'(C_i) = \frac{N_i^{prod}}{\sum_{j=1}^{n_I} N_j^{prod}}. \tag{8.5}$$

Then the N_{diff}^{prod} in (8.4) and the N_{diff}^{prod} obtained in the previous iteration are compared. If the χ^2/ndf for the difference becomes stable, the obtained N_{diff}^{prod} is regarded as reliable and the iterative procedure is stopped. Otherwise, the probability $P_0(C_i)$ is replaced by the $P_0'(C_i)$ and the procedure from (8.2) is repeated until the result becomes stable.

In this analysis, the N_{diff}^{prod} is obtained after two iterations.

8.1.2 Inclusive diffractive cross section

In this section, the inclusive diffractive cross section, $d\sigma_{\gamma^* p}^{diff}/dM_X$, is extracted from the N_{prod}^{diff} obtained above.

The N_{prod}^{diff} is directly connected to the ep cross section, thus it will be translated into the $\gamma^* p$ cross section using the relation (2.19). However, it is necessary to take into account the radiative effect before making use of the relation (2.19). The Born ep cross section for each bin is calculated as

$$\frac{d\sigma_{ep}^{diff}}{d\ln Q^2 d\ln W dM_X} = \frac{1}{\mathcal{L}} \cdot \frac{N_{prod}^{diff}}{\Delta\ln Q^2 \Delta\ln W \Delta M_X} \cdot \frac{\sigma_{Born}}{\sigma_{rad}} \tag{8.6}$$

where $\mathcal{L}$ is the integrated luminosity, 2.433pb^{-1}. The $\Delta\ln Q^2$, ΔW and ΔM_X are widths of the bins. Both the radiative cross section (σ_{rad}) and Born cross section (σ_{Born}) are calculated with HERACLES.

In the recent ZEUS results of the exclusive ρ^0 production[74], the Q^2 dependence of $R = \sigma_L/\sigma_T$ is fitted to the form, κQ^2, and it gives: $\kappa = 0.81 \pm 0.05(stat) \pm 0.06(syst)$ GeV^{-2}. Even if this is taken into account, the factor $(1+R^{diff})/(1+\epsilon R^{diff})$ in (2.19) can be approximated to unity because $\epsilon \simeq 1$ in the considered y range. The deviation of the factor from unity is less than 3% for all the W bins. Therefore, the $\gamma^* p$ diffractive cross section can be obtained as

$$\frac{d\sigma_{\gamma^* p}^{diff}}{dM_X} = \frac{\pi}{\alpha} \cdot \frac{1}{1+(1-y)^2} \cdot \frac{d\sigma_{ep}^{diff}}{d\ln Q^2 d\ln W dM_X} \tag{8.7}$$

from the relation (2.19). The y is calculated from the relation, $y = W^2/s$, where W is the center value of $\ln W$ for each bin.

Fig. 8.1 shows the inclusive diffractive cross section, $d\sigma_{\gamma^* p}^{diff}/dM_X$, as a function of W for each Q^2 and M_X region. The inner error bars show the statistical errors and the full bars are the statistical and systematic errors added in quadrature. The estimation of the systematic errors are described in the next section.

8.1.3 Systematic errors

The sources of the systematic errors for the diffractive cross section can be classified into two groups; the one is originated from the positron measurement and the other is related to the hadronic final states. The check items for each group are briefly summarized in Tab. 8.1. The whole analysis procedures are repeated for the individual error sources as described below. The systematic errors are put according to the variations of the cross sections.

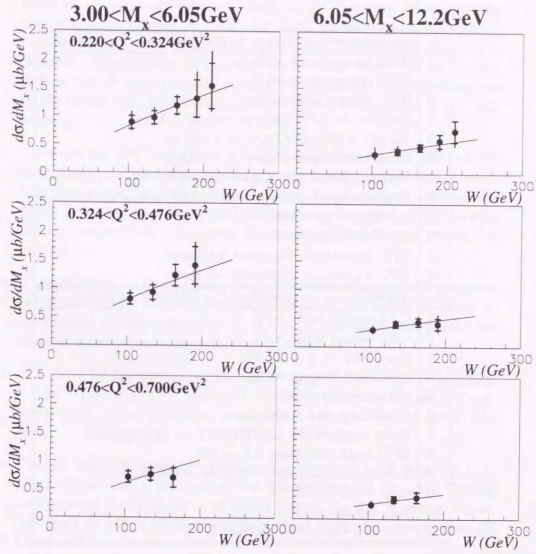

Fig. 8.1: The diffractive cross section, $d\sigma_{\gamma^* p}^{diff}/dM_X$, as a function of W for each Q^2 and M_X region. The inner error bars show the statistical errors and the full bars are the statistical and systematic errors added in quadrature. The curves show the results of the fit to the form (8.12).

A: Systematic errors related to the positron measurement	
1	BPC energy scale +1%
2	BPC energy scale −1%
3	BPC energy uniformity
4	Shrinks the BPC fiducial volume −0.5cm
5	Shower width, σ <7mm $\rightarrow$ σ <8mm
6	Shower width, σ <7mm $\rightarrow$ σ <6mm
7	Positron beam tilt, θ_{tilt} =0.27mrad $\rightarrow$ θ_{tilt} =0.08mrad
8	Positron beam tilt, θ_{tilt} =0.27mrad $\rightarrow$ θ_{tilt} =0.46mrad
9	ω_0 =2.8 $\rightarrow$ ω_0 =3.0
10	ω_0 =2.8 $\rightarrow$ ω_0 =2.6
11	BPC x position alignment +0.5mm
12	BPC x position alignment −0.5mm
B: Systematic errors related to the hadronic final states	
1	CAL energy scale +3%
2	CAL energy scale −3%
3	y_{JB} >0.05 $\rightarrow$ y_{JB} >0.04
4	y_{JB} >0.05 $\rightarrow$ y_{JB} >0.06
5	Vertex requirement
6	δ >35GeV $\rightarrow$ δ >40GeV
7	Noise suppression 120/160MeV $\rightarrow$ 140/160MeV
8	EFO track selection: 0.8 $\rightarrow$ 0.9
9	EFO probability cut: 0.2/0.05 $\rightarrow$ 0.3/0.1
10	b_{nom} =1.39+0.03
11	b_{nom} =1.39−0.03
12	The M_X correction method B

Tab. 8.1: The sources of systematic errors. The items in the upper and lower half of the table denote the errors related to the positron measurement and hadronic final states, respectively.

Systematic errors related to the positron measurement:

- In section 5.3.3, the uncertainty of the BPC absolute energy scale was taken as 1% using the elastic ρ^0 candidates. Therefore, after changing the BPC strip energy by ±1%, the BPC reconstruction is repeated only for data. In most of the bins, the cross section changes within 5%. However, changing the BPC energy scale brings about the systematic shift in the W distributions; it could be significant for extracting the $\alpha_{I\!P}(0)$ rather than for the cross section. It will be discussed in the next section.

- Although the BPC energy uniformity was measured to be within 0.5% as seen in Fig. 5.2, an effect of the radiation damage is to be considered[62]. It is done by multiplying a linear function of x position to scale up and down the energy by 0.5% at the inner and outer end of the BPC fiducial volume, respectively. Typically, the cross sections change only a few percent.

- If the material in front of the BPC is not described in MC properly, the result of the unfolding would be affected. In order to check it, the fiducial volume is shrinked by 0.5cm. In particular, the results are changed largely (from 15 to 20%) in the high Q^2 region.

- The value for the shower width cuts is changed from 7mm to 8(6)mm. In the higher M_X bins, the cross section is increased(decreased) systematically, while almost no changes are observed in the lower M_X bins.

- The tilt angle of the positron beam, ϑ_{tilt}, is determined from Fig. C.2, which shows the x position of the bremsstrahlung photon. Taking into account the RMS value of about 20mm, the ϑ_{tilt} is changed from 0.27mrad to 0.08(0.46)mrad. It is sensitive in the low and middle Q^2 bins (~5%).

- The position of the scattered positron is measured using the logarithmic weighted method (5.4) and (5.6) where the weighting factor is determined as (5.5). The ω_0 in (5.5) is changed from 2.8 to 3.0(2.6)[62, 63]. It tends to raise(lower) the cross section by a few percent in the higher M_X bins.

- As mentioned in Section 5.3.5, the absolute position of the BPC module was measured with an accuracy of 0.5mm. From the survey, the module is horizontally 4.38cm away from the beam axis. In the calculation

of the scattered angle of the positron, the distance 4.38cm is varied ±0.5mm. It increases(decreases) the cross section systematically about 5% at low Q^2, but the variation becomes small in the higher Q^2 bins.

Systematic errors related to the hadronic final states:

- The CAL energy scale uncertainty of ±3% is taken into account[75]. The scale is changed accordingly for data. After scaling up(down) the CAL energy, the M_X is reconstructed larger(smaller) and the cross section is increased(decreased) systematically.
- To check the influence of the migration from the lower W region due to the initial state radiation, the threshold of the y_{JB} cut is changed from 0.05 to 0.04(0.06). In most of the bins, little changes are seen. Only in the highest Q^2, W and M_X bin, the cross section is changed about 10%.
- The whole procedure is repeated restricting the events with the CTD vertex. However, the cross sections in higher(lower) W bins tend to decrease(increase) and deviations amounts to 20% depending on bins. This varies the W slopes of the cross sections, that is, the extracted value of $\alpha_{I\!P}(0)$ is reduced significantly. This is discussed further in the next section again.
- To check the influence of the additional photoproduction backgrounds, the cut value of the $\delta = E - p_z$ is raised from 35GeV to 40GeV. Except the lowest Q^2 and the highest W (22%), the variation is less than 2% in the lower M_X bins. In the higher M_X bins, it is at most 7%.
- The energy threshold for isolated EMC cells is raised from 120MeV to 140MeV. The variation is within 5% except the lowest Q^2 and the highest W (11%).
- The criteria (D.2), which is for selecting one of the track or the island, is altered to take more tracks by changing the value of 0.8 to 0.9. Although the cross sections are increased about 3.5% in the high Q^2 and M_X bins, they are changed less than 2% in other bins.
- The probability cuts for merging cell islands to a cone island is changed from 0.2/0.05 to 0.3/0.1. This almost does not change the results.

Q^2 (GeV^2)	W (GeV)	Diffractive Cross Section, $\frac{d\sigma}{dM_X}$ (μb/GeV)	
		3.00< M_X <6.05(GeV)	6.05< M_X <12.2(GeV)
0.222 - 0.324	90 - 120	$0.886 \pm 0.115^{+0.161}_{-0.098}$	$0.341 \pm 0.050^{+0.120}_{-0.074}$
	120 - 150	$0.970 \pm 0.118^{+0.133}_{-0.046}$	$0.389 \pm 0.055^{+0.097}_{-0.028}$
	150 - 180	$1.181 \pm 0.153^{+0.109}_{-0.091}$	$0.463 \pm 0.063^{+0.053}_{-0.045}$
	180 - 200	$1.307 \pm 0.327^{+0.341}_{-0.113}$	$0.580 \pm 0.121^{+0.041}_{-0.120}$
	200 - 220	$1.532 \pm 0.401^{+0.465}_{-0.211}$	$0.749 \pm 0.191^{+0.075}_{-0.185}$
0.324 - 0.476	90 - 120	$0.808 \pm 0.097^{+0.114}_{-0.037}$	$0.295 \pm 0.043^{+0.070}_{-0.048}$
	120 - 150	$0.922 \pm 0.128^{+0.117}_{-0.111}$	$0.391 \pm 0.056^{+0.071}_{-0.026}$
	150 - 180	$1.226 \pm 0.189^{+0.070}_{-0.082}$	$0.432 \pm 0.073^{+0.074}_{-0.032}$
	180 - 200	$1.402 \pm 0.328^{+0.244}_{-0.213}$	$0.395 \pm 0.100^{+0.140}_{-0.099}$
0.476 - 0.700	90 - 120	$0.710 \pm 0.102^{+0.103}_{-0.040}$	$0.250 \pm 0.049^{+0.061}_{-0.032}$
	120 - 150	$0.764 \pm 0.110^{+0.094}_{-0.091}$	$0.349 \pm 0.058^{+0.040}_{-0.058}$
	150 - 180	$0.705 \pm 0.169^{+0.144}_{-0.084}$	$0.380 \pm 0.092^{+0.076}_{-0.045}$

Tab. 8.2: The diffractive cross section in low Q^2 region. The first and second error values represent the statistical and systematic errors, respectively.

- The non-diffractive backgrounds are subtracted with the b_{nom} of 1.39+0.03 and 1.39−0.03 where 0.03 is the statistical error of the slope. In higher M_X bins, it causes shallower(steeper) W dependence of $d\sigma^{diff}_{\gamma^* p}/dM_X$, which results in extracting the smaller(larger) $\alpha_{I\!P}(0)$ as discussed in the next section.
- The M_X correction method B is adopted before the non-diffractive subtraction. In the lowest W and higher M_X bins, the cross sections are changed as much as 10%.

Fig. 8.2 to 8.4 show the relative difference of the cross sections for each source of systematic errors discussed above. The horizontal axis indicates the labels of error sources which are given in Tab. 8.1. Finally, the obtained values of the diffractive cross sections are summarized in Tab. 8.2 with statistical and systematic errors. The systematic errors are determined by adding the errors from different sources in quadrature separately for the positive and negative contributions.

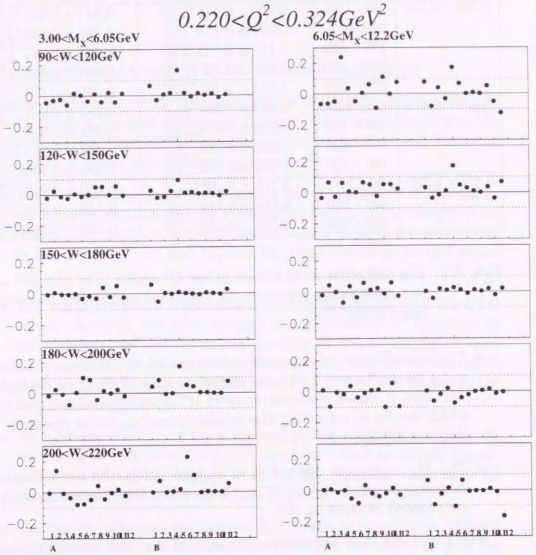

Fig. 8.2: The systematic errors for the diffractive cross section, $d\sigma^{diff}_{\gamma^* p}/dM_X$, in the Q^2 region of $0.220< Q^2 <0.324\text{GeV}^2$. The vertical axis shows the relative difference of the cross sections for each source of systematic errors.

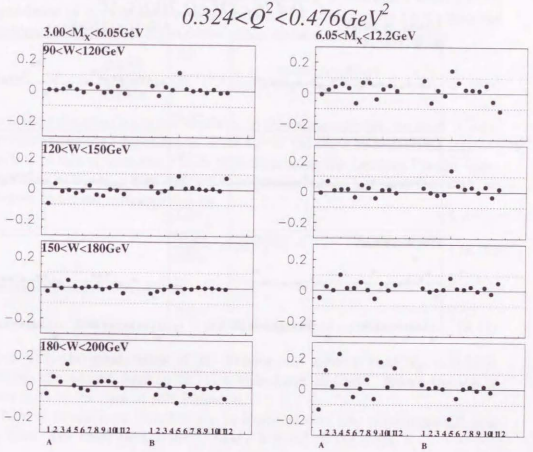

Fig. 8.3: The systematic errors for the diffractive cross section, $d\sigma^{diff}_{\gamma^* p}/dM_X$, in the Q^2 region of $0.324< Q^2 <0.476\text{GeV}^2$. The vertical axis shows the relative difference of the cross sections for each source of systematic errors.

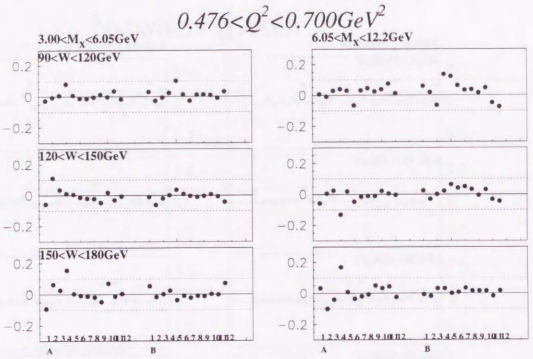

Fig. 8.4: The systematic errors for the diffractive cross section, $d\sigma^{diff}_{\gamma^* p}/dM_X$, in the Q^2 region of 0.476< Q^2 <0.700GeV^2. The vertical axis shows the relative difference of the cross sections for each source of systematic errors.

8.2 Extraction of $\alpha_{I\!P}(0)$

Finally, the intercept of the Pomeron trajectory is extracted from the W dependence of the diffractive cross section. By substituting (2.30) into the equation (2.34), the W dependence of the cross section is derived as

$$\frac{d^2\sigma^{diff}_{\gamma^* p}}{dtdM_X} \propto (W^2)^{2\alpha_{I\!P}(0)-2} \cdot e^{t(b+2\alpha'_{I\!P} ln \frac{W^2}{M_X^2+Q^2})}. \tag{8.9}$$

Since the t distribution is not available in this measurement, we need to integrate assuming the t dependence. Here we use the slope of 7.5±1.1±1.1GeV^{-2}[76] which is obtained from the ZEUS 1995 data using the Leading Proton Spectrometer (LPS)[69]. The diffractive cross section is now written with an effective Pomeron intercept $\bar{\alpha}_{I\!P}$ as

$$\frac{d\sigma^{diff}_{\gamma^* p}}{dM_X} \propto (W^2)^{2\bar{\alpha}_{I\!P}-2}. \tag{8.10}$$

The $\bar{\alpha}_{I\!P}$ is related to $\alpha_{I\!P}(0)$ as

$$\bar{\alpha}_{I\!P} = \alpha_{I\!P}(0) - \alpha'_{I\!P} \cdot |\bar{t}| \tag{8.11}$$

where $|\bar{t}|$ is the mean value of $|t|$. Taking into account that $\alpha'_{I\!P} = 0.25 \pm 0.02$[39], the second term in (8.11) is calculated as 0.033. Hence the $\bar{\alpha}_{I\!P}$ is about 1.05 in the case of soft Pomeron.

Now it is assumed that the $\bar{\alpha}_{I\!P}$ is identical over the considered Q^2 and M_X bins. The cross section $d\sigma^{diff}_{\gamma^* p}/dM_X$ is fitted to the form,

$$\frac{d\sigma^{diff}_{\gamma^* p}}{dM_X} = A \cdot W^{2(2\bar{\alpha}_{I\!P}-2)} \tag{8.12}$$

for each Q^2 and M_X bin. The curves in Fig. 8.1 are the result of the fit and the effective Pomeron intercept is extracted as $\bar{\alpha}_{I\!P}$=1.184±0.026(stat).

The above procedure is repeated after every systematic variation listed in Tab. 8.1. The obtained values of $\bar{\alpha}_{I\!P}$ are shown as closed circles in Fig. 8.5 with statistical errors. The labels along the horizontal axis represent the sorts of error sources.

Among the error sources related to the positron measurement, it is expected that the largest variation of W dependence could come from the BPC absolute energy scale (A1 and A2). If the energy scale is raised(lowered), the W tends to be reconstructed smaller(larger) and it results in shallower(steeper) W dependence of the diffractive cross section. However, the deviation from

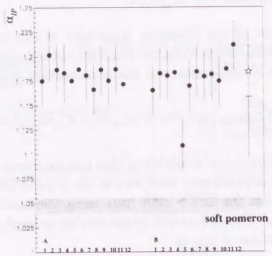

Fig. 8.5: The extracted effective Pomeron intercept. The labels represent the sorts of systematic errors seen in Tab. 8.1.

the nominal value of $\bar{\alpha}_{I\!P}$ is within the statistical error. It is also the case for the others related to the positron measurement.

In the rest of the error sources, the vertex requirement (B5) apparently reduced the value of $\bar{\alpha}_{I\!P}$. The difference amounts to as large as 2σ of the statistical error. There are two possible reasons; one of them is the remaining beam-gas backgrounds and the other is the uncertainty of the vertex finding efficiency. In order to check the first possibility, the whole analysis procedure has been repeated without the beam-gas subtraction using pilot bunches described in Section 7.6.1. Then, we obtain that $\bar{\alpha}_{I\!P} = 1.180 \pm 0.026$, which is consistent with the nominal value. In order to investigate the second possibility, the charged track multiplicity is compared between the data and MC in Appendix F. Fig. F.1 shows the number of CTD tracks after selecting the events with $\ln M_X^2 < 5$; the dots and histograms represent the data and MC, respectively. Selecting the events with CTD vertex corresponds to removing the events with no tracks in CTD. As seen in the figure, the MC does not describe the data where the number of tracks is equal to 0 or 1. The discrepancy is accompanied by the W dependence. The vertex finding efficiency becomes worse as W increases and the W dependence in the data is more rapid than that in the MC. This causes the slower W dependence of the diffractive cross section and reduces the value of extracted $\bar{\alpha}_{I\!P}$. Thus,

Photoproduction		
Q^2(GeV^2)	$\alpha_{I\!P}(0)$	
0	1.12±0.04(stat)±0.08(syst)	ZEUS[15]
0	1.068±0.016(stat)±0.022(syst)±0.041(model)	H1[16]
THIS ANALYSIS		
Q^2(GeV^2)	$\alpha_{I\!P}(0)$	
0.220 - 0.700	$1.217\pm0.026(\text{stat})^{+0.042}_{-0.088}(\text{syst})$	ZEUS
DIS		
Q^2(GeV^2)	$\alpha_{I\!P}(0)$	
7 - 140	$1.16\pm0.01(\text{stat})^{+0.04}_{-0.01}(\text{syst})$	ZEUS[23]
4.5 - 75	$1.203\pm0.020(\text{stat})\pm0.013(\text{syst})^{+0.030}_{-0.035}(\text{model})$	H1[24]

Tab. 8.3: The results of the intercept of Pomeron trajectory in different Q^2 regions.

the extracted value of $\bar{\alpha}_{I\!P}$ is sensitive to the difference of the vertex finding efficiency between the data and MC. We do not adopt the vertex requirement in the main analysis but the variation from the nominal $\bar{\alpha}_{I\!P}$ is included in the systematic error.

The systematic error on $\bar{\alpha}_{I\!P}$ is evaluated by adding the deviations from the nominal $\bar{\alpha}_{I\!P}$ in quadrature separately for the positive and negative contributions. Then we obtain the effective Pomeron intercept as

$$\bar{\alpha}_{I\!P} = 1.184 \pm 0.026(stat)^{+0.042}_{-0.088}(syst) \tag{8.13}$$

and it can be seen as a star in Fig. 8.5. As seen in Fig. 8.5, the extracted $\bar{\alpha}_{I\!P}$ is significantly higher than that of soft Pomeron.

Finally, the value of 0.033 for the second term in (8.11) is added to the $\bar{\alpha}_{I\!P}$ to obtain the intercept of Pomeron trajectory, $\alpha_{I\!P}(0)$, at 0.220< Q^2 <0.700GeV^2. The result is:

$$\alpha_{I\!P}(0) = 1.217 \pm 0.026(stat)^{+0.042}_{-0.088}(syst). \tag{8.14}$$

It is consistent with $\alpha_{I\!P}(0)$ =1.141±0.020(stat)±0.044(syst), which was obtained from the W dependence of the $\gamma^* p$ total cross section in the Q^2 range of 0.11< Q^2 <0.65GeV^2[20]. The values of $\alpha_{I\!P}(0)$ obtained from this analysis and reference [20] are shown as a star and a closed circle in Fig. 8.6.

The result is compared with those from the other Q^2 regions, which are summarized in Tab. 8.3. Those results are also shown in Fig. 8.6. For comparison, the curve in the figure shows the $\alpha_{I\!P}(0)$ obtained from the ALLM

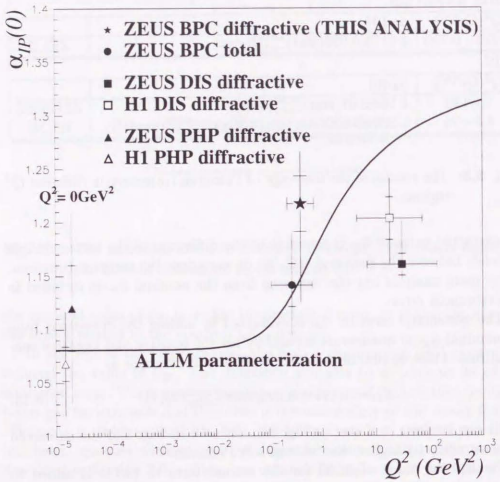

Fig. 8.6: The intercept of Pomeron trajectory as a function of Q^2. The values of $\alpha_{I\!P}(0)$ obtained from this analysis and the $\gamma^* p$ total cross section are shown as a star and a closed circle. The triangles and squares show the results obtained from the photoproduction and DIS diffractive events, respectively. The curve is obtained from the ALLM parameterization.

parameterization, which is a parameterization for describing the $\gamma^* p$ total cross section[77, 78]. It is based on the Regge motivated parameterization and extended to the higher Q^2 region being compatible with the QCD expectation. The total cross sections obtained from BPC data are also used for the fit.

The $\alpha_{I\!P}(0)$ in photoproduction was determined from the shape of M_X distribution[15, 16]. As seen in Tab. 8.3, both results are consistent with that of soft Pomeron. On the other hand, in DIS ($Q^2 \gg 1\,\mathrm{GeV}^2$), ZEUS[23] extracted $\alpha_{I\!P}(0)$ from the $\ln M_X^2$ distributions and H1[24] looked into the $x_{I\!P}$ dependence of the diffractive structure function. The $\alpha_{I\!P}(0)$ from both experiments are significantly higher than that of soft Pomeron. In the Regge theory, the W dependence of the diffractive cross section should be related with that of the total cross section in terms of $\alpha_{I\!P}(0)$. However, as shown in the figure, the $\alpha_{I\!P}(0)$ from the DIS diffractive events is incompatible with that is expected from the W dependence of the total cross section.

In this thesis, we obtain the $\alpha_{I\!P}(0)$ as (8.14) from the diffractive events in the Q^2 transition region between photoproduction and DIS. In contrast to the results in DIS, it is consistent with the value obtained from the $\gamma^* p$ total cross section in the same Q^2 range. However, the obtained value turned out to be significantly higher than the soft Pomeron and much closer to the results from the large Q^2 region. The steeper W dependence compared with the expectation from the naive Regge phenomenology suggests the contribution from hard processes also in the low Q^2 diffractive scattering.

9. Conclusions

The cross section of the diffractive process, $\gamma^* + p \rightarrow X + N$, has been measured in the mass range, 3< M_X <12.2GeV and M_N <6GeV for the low Q^2 region, 0.220< Q^2 <0.700GeV^2, and 90< W <220GeV.

The low Q^2 region was explored by detecting the scattered positron using the BPC. From the measured energy and position of the scattered positron, the kinematic variables, Q^2 and W, were reconstructed according to the electron method.

The mass of the photon dissociated system, M_X, was reconstructed from the energy flow objects which the CAL energy deposits and CTD tracks were clustered into. Taking advantage of the difference of the $\ln M_X^2$ distributions between the diffractive and non-diffractive processes, the non-diffractive contribution was subtracted statistically from the inclusive low Q^2 event sample.

The measured number of diffractive events was translated into the diffractive cross section, $d\sigma^{diff}_{\gamma^* p}/dM_X$, by taking into account the detector effect and the QED radiative correction. The cross sections for the Q^2 and M_X regions are shown in Fig. 8.1 as a function of W and the values of them are tabulated in Tab. 8.2 with the statistical and systematic errors.

The intercept of Pomeron trajectory was extracted from the W dependence of the diffractive cross section. The obtained value is

$$\alpha_{\mathbb{P}}(0) = 1.217 \pm 0.026(stat)^{+0.042}_{-0.088}(syst).$$

It is consistent with the result obtained from the measurement of the $\gamma^* p$ total cross section in the same Q^2 range. It turns out to be significantly higher than 1.08 that is expected from the soft Pomeron. The steeper W dependence compared with the expectation from the naive Regge phenomenology suggests the contribution from hard processes also in the low Q^2 diffractive scattering.

Acknowledgements

Thanks to the precious experience at DESY and the great help of many people, I could carry out the analysis described in this thesis.

First of all, I am most grateful to Prof. S. Yamada that he gave me the opportunity to study the high energy physics in the ZEUS collaboration. He also gave me the theme of this thesis and everything started from his precious suggestion.

I wish to express my special thanks to Prof. K. Tokushuku who gave me the valuable advice throughout my work. Without his advice and discussions with him, I could not carry out my analysis at all. Furthermore, I really appreciate his careful reading of the draft and giving lots of useful comments on it.

Working on the physics analysis in the ZEUS diffractive group was a wonderful experience. Especially, I would like to thank the coordinators of the group, Prof. H. Abramowicz and Dr. K. Piotrzkowski, who introduced me to diffraction, gave me valuable advice and supported my studies over all the subjects described below.

I would like to thank people in the BPC group. In particular, I have learned not only the details of BPC reconstruction but also the exciting aspects of the low Q^2 physics from Dr. Q. Zhu, Dr. B. Surrow and Dr. T. Monteiro since I began to work in the collaboration. I am grateful to Mr. U. Fricke, Mr. V. Monaco, Mr. D. Kcira and Mr. C. Amelung for their technical help of the BPC reconstruction and in situ BPC calibration. I would also like to thank Dr. A. Quadt and Dr. A. Pellegrino for organizing the BPC analysis meeting.

The development of MC simulation is one of my important works. First, I am indebted to Dr. M. Kasprzak who provided the prototype of EPSOFT. I would also like to thank Mr. R. Cross, Dr. W. N. Murray, Mr. M. St-Laurent, Dr. C. M. Ginsburg and Dr. J. Figiel for testing my code and giving useful comments and suggestions. Moreover, I would like to express my special thanks to Ms. K. Klimek for the discussions about particle multiplicity and lots of encouragement till the end of writing this thesis.

The method of extracting the diffractive events is the dominant part in my analysis procedure. I wish to acknowledge that I could acquire the essential knowledge and techniques through the discussions with leading experts. Dr. G. Wolf, Dr. H. Kowalski, Dr. L. Lindeman and Ms. B. Smalska. I would also like to thank Prof. M. Arneodo, Dr. M. Capua and Mr. B. Mellado for the information about the LPS measurement and the BPC total cross section.

It was a great opportunity to participate in the construction of the Forward Plug Calorimeter (FPC). I enjoyed working with Dr. M. Kasemann, Mr. F. Goebel and other colleagues sharing the time for the test beam at CERN.

I would like to thank Prof. I. H. Park for his useful comments on my work while he visited Japan. I also acknowledge Mr. C. Chung, Ms. H. Lim and Ms. K. Ma for their friendship.

I wish to acknowledge all the members of the ZEUS Tokyo group.

Especially, Dr. M. Kuze supported me during my stay at DESY. His pertinent advice always led me to the right way. I would like to acknowledge valuable discussions with Dr. Y. Yamazaki who has been continuously showing us what a physicist is to be.

I would like to express great thanks to Mr. K. Umemori and Mr. K. Nagano who have been good friends as well as good collaborators. I was always encouraged when I saw them working hard.

I wish to acknowledge all the valuable discussions at the ZEUS Tokyo meeting with Prof. R. Hamatsu, Dr. T. Ishii, Dr. S. Kitamura, Dr. T. Tsurugai, Dr. M. Iga, Dr. I. Fleck, Dr. M. Nakao, Dr. I. Suzuki, Dr. S. Mine, Dr. K. Homma, Dr. K. Yamauchi, Dr. T. Matsushita, Mr. T. Abe, Mr. T. Yamashita, Mr. T. Fusayasu, Mr. T. Nishimura, Mr. G. Sato and other colleagues.

I would also like to thank friends in KEK-IPNS, Mr. N. Muramatsu, Mr. T. Tamagawa, Mr. Y. Tagaya and Mr. J. Nakano for making my graduate student period fruitful.

Last but not least, I would like to express my gratitude to my family. Thanks to their continuous support and encouragement, I could carry out the study and have such precious experiences for my life.

Appendix

A. The BPC energy uniformity

Fig. A.1 shows the kinematic region on the $x-Q^2$ plane. The diagonal dotted lines indicate constant y; $y = 1$ is the kinematical limit and we can explore only the region below the line. The area between thick solid curves is the geometrical acceptance of BPC. The thin curves are contours of $E_{e'}$ =27 and 28 GeV.

Fig. A.1 shows that the energy of the scattered positron is close to the incoming positron energy for the events with $y \ll 1$. These events are suitable for a detector calibration. In this thesis, events whose y is smaller than 0.04 are defined as the kinematic peak (KP) events. The events are regarded as the KP events if they satisfy the following conditions[79].

- The local position of a candidate for a scattered positron should be reconstructed in the BPC fiducial volume.
- The dispersion, σ_x and σ_y from equations (5.7) and (5.8), should be less than 0.7cm.
- The y_{JB} defined in (5.19) should be less than 0.04.
- The δ defined in (5.20) is required to be greater than 50GeV.

In Fig. 5.2, the mean value of the measured energy is scanned horizontally and vertically with KP events. Vertical lines exhibit the BPC fiducial volume and strip boundaries. The horizontal broken lines represent $\pm 0.5\%$ deviations from the average energy. From the figures, the energy uniformity inside the fiducial volume is guaranteed within 0.5% level.

As well as the uniformity, the absolute energy scale of BPC was adjusted with KP events by comparing the BPC energy distributions of the data and MC events[62, 63, 64]. This was done by searching for the values of c_x and c_y in (5.10) which minimize,

$$\chi^2 = \sum_{bins} \frac{(N_{DATA} - N_{MC})^2}{\sigma^2_{DATA} + \sigma^2_{MC}}. \tag{A.1}$$

Fig. A.2 show the BPC energy distributions of KP events after the whole calibration procedure. The dots and histogram represent the data and MC, respectively.

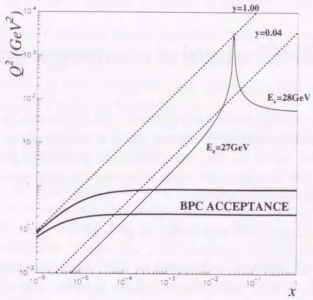

Fig. A.1: The kinematic phase space on the $x - Q^2$ plane.

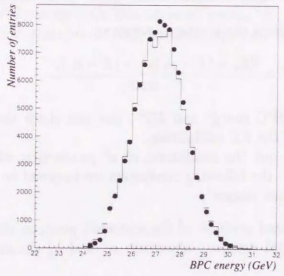

Fig. A.2: Energy distributions of KP events. The dots and histogram mean the data and MC, respectively.

B. The BPC absolute energy scale

The BPC absolute energy scale was adjusted with KP events in Appendix A. However, one might wonder if the energy scale is reliable because the above calibration method relied on MC simulation. It would be good to confirm the reliability of the energy scale with independent data sample. For this purpose, the elastic ρ^0 production:

$$e^+ + p \longrightarrow e^+ + \rho^0 + p \tag{B.1}$$

where the scattered positron is detected in BPC and two pions from ρ^0 are identified in CTD, is a suitable process. This is because the energy of the scattered positron is calculable from momenta of pions and scattered angle of the positron. Considering the conservation of $E - p_z$ through the ρ^0 production,

$$\begin{aligned} 2E_e &= (E-p_z)_{e^+} + (E-p_z)_{\rho^0} + (E-p_z)_p \\ &\simeq E_{e'}(1-\cos\theta_{e'}) + (E-p_z)_{\pi^+} + (E-p_z)_{\pi^-} \end{aligned} \tag{B.2}$$

it is possible to calculate the positron energy as

$$E_{e'}^{calc} = \frac{2E_e + (E-p_z)_{\pi^+} + (E-p_z)_{\pi^-}}{1-\cos\theta_{e'}}. \tag{B.3}$$

By comparing the BPC energy and $E_{e'}^{calc}$, one can check the BPC energy scale independent of the KP calibration.

In order to pick out the candidates of ρ^0 production whose scattered positron enters BPC, the following conditions are imposed on the data triggered by BPC inclusive trigger[1].

- The reconstructed position of the scattered positron should be inside the BPC fiducial volume. Moreover, σ_x and σ_y should be less than 7mm.
- The δ should be greater than 50GeV.

[1] The BPC inclusive trigger is explained in Chapter 6.

- The y_{JB} should be greater than 0.02. This cut is required because a similar condition is already included in the BPC inclusive trigger.
- The number of charged tracks associated with the event vertex should be exactly 2. In addition, they should have opposite charges each other.
- The ratio of the total energy in CAL and sum of momenta of 2 tracks, E_{CAL}/p_{tracks}, should be less than 1.5.
- Assuming the tracks are pions, the invariant mass, $m_{\pi\pi}$, should be between 0.57 and 0.97 GeV.

Fig. B.1(a) is the distribution of invariant mass of 2 tracks found in CTD. The events in the mass window shown as a shaded histogram are taken to check the BPC energy scale. Fig. B.1(b) is the BPC energy spectrum of the selected ρ^0 candidates. Since the peak position is slightly lower than that of KP events seen in Fig. A.2, the reliability of the BPC energy scale can be examined in the different energy region. Fig. B.1(c) shows the ratio of the measured BPC energy and calculated energy. The dots and histogram represent results from the data and MC, respectively. The agreement between them is fairly good. As seen in the figure, the ratio is fitted with Gaussian and the obtained mean value is 0.989 for the data. It is slightly less than unity because of the remaining radiative correction. Since the mean value of 0.996 is obtained from the elastic ρ^0 MC with radiative correction, it turned out that the BPC energy scale was adjusted within 1%. This uncertainty of 1% is taken into account when the systematic errors are estimated in Chapter 8.

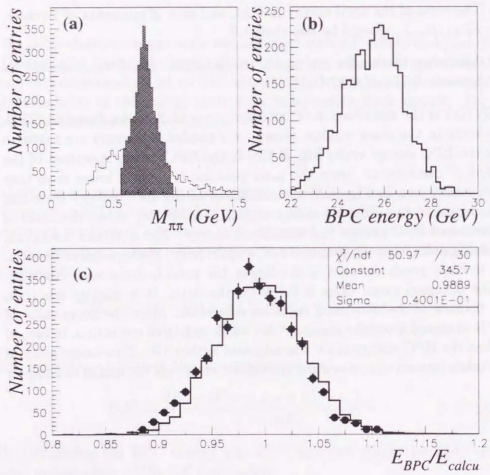

Fig. B.1: (a)The invariant mass of 2 tracks. The mass window between 0.57 and 0.97 GeV (shaded histogram) represents the ρ^0 candidates. (b)The BPC energy distribution of ρ^0 candidates. (c)The ratio of the BPC measured energy and calculated energy. The dots and histogram are results from data and MC, respectively.

C. Tilt of positron beam

From the equations (5.10) and (5.14), we know the energy and polar angle of the scattered positron. Now it seems to be possible to calculate the relevant kinematic variables by substituting them into equations from (5.1) to (5.3). However, before calculations, the tilt of the positron beam also has to be taken into account because they were formulated on the assumption that the initial state positron is parallel to the z-axis of ZEUS coordinate.

It is observed from the emission angle of the photon from bremsstrahlung process,

$$e^+ + p \longrightarrow e^+ + \gamma + p. \tag{C.1}$$

Since such a photon goes almost straight along the positron beam direction, the tilt angle can be measured by looking at the hit position on the LUMIG counter which sits at $z = -107$m and detects bremsstrahlung photons.

Fig. C.1 shows the top view of the LUMIG counter and proton orbit. The value of x hit position on LUMIG, x_{lumi}(mm), was recorded as a distance from the proton orbit which is also drawn in the figure. From the survey, the proton orbit is known to be tilted 0.41mrad from ZEUS z-axis towards the center of the HERA ring. Therefore, the tilt angle ϑ_{tilt}(mrad) is obtained from the following relation,

$$\vartheta_{tilt} = 0.41 + \frac{x_{lumi}}{107}. \tag{C.2}$$

Fig. C.2 is the x_{lumi} distribution of bremsstrahlung photons at the LUMIG counter. As shown in the figure, the mean value of x_{lumi} turned out to be -14.58mm during the 1996 data taking. That is, ϑ_{tilt} is obtained as 0.27mrad.

Taking into account the beam tilt, the momentum of the initial positron can be expressed as

$$\begin{aligned} k_i &= (\Delta p_x, 0, -E_e, E_e) \\ &= (0, 0, -E_e, E_e) + (\Delta p_x, 0, 0, 0) \\ &= k_i^o + \Delta k \end{aligned} \tag{C.3}$$

where $\Delta p_x = E_e \cdot \tan\vartheta_{tilt} = 0.0075$(GeV). The first term in (C.3) is the initial momentum without the beam tilt and the second term represents the

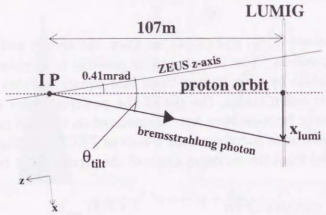

Fig. C.1: Top view of the LUMIG counter and proton orbit.

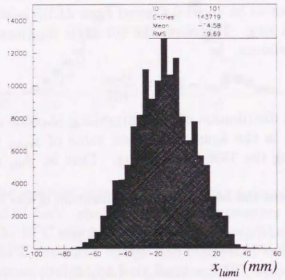

Fig. C.2: The x-position of bremsstrahlung photons at the LUMIG counter.

deviation due to the tilt. From (C.3) and the momentum of the final state positron:

$$k_f = (E_{e'} \sin\theta_{e'} \cos\phi_{e'}, E_{e'} \sin\theta_{e'} \sin\phi_{e'}, E_{e'} \cos\theta_{e'}, E_{e'}), \tag{C.4}$$

the corrected Q^2 can be obtained as

$$\begin{aligned} Q^2 &= -(k_i - k_f)^2 \\ &= -(k_i^o - k_f)^2 - 2\Delta k \cdot (k_i^o - k_f) \\ &= Q_o^2 + 2\Delta p_z \sin\theta_{e'} \cos\phi_{e'}. \end{aligned} \tag{C.5}$$

Similarly the first term is Q^2, which is calculated using the equation (5.1), and the second one is the correction term for the beam tilt effect.

For the calculation of W, the effect of the tilt is negligible because W is characterized mainly by $E_{e'}$ and insensitive to the small change of $\theta_{e'}$ as seen in the formulae (5.2) and (5.3).

D. Energy flow objects

The energy flow objects are formed from the CAL energy deposits and the CTD tracks according to the following procedure.

1. After the noise suppression mentioned in Section 5.4.2, neighboring energetic cells in CAL are grouped into clusters as follows.

   (a) At first, adjacent cells are gathered around the local maxima as depicted in Fig. D.1. This clustering is done separately in each section (EMC, HAC1 and HAC2) in FCAL, BCAL and RCAL. The resulted cluster is called 'cell island'. The local positions of cell islands are calculated from coordinates of contained cells by weighting their energy logarithmically.

   (b) The opening angles between cell islands are calculated. Then the angles are translated into the probability that those cell islands are originated from one particle. The probability functions were obtained using single pion MC events[80] and they are shown in Fig. D.2 as a function of the opening angle. The solid line is for pairs of HAC-HAC cell islands and broken line is for HAC-EMC and EMC-EMC.

   (c) If the probability is larger than the minimum values, they are merged into one 'cone island'. The minimum probability is set to 0.2 for EMC-EMC pairs and set to 0.05 for other pairs of cell islands.

   (d) The positions of the cone islands are recalculated from coordinates of contained cells by weighting their energy logarithmically.

   (e) Suppose there is a cone island composed of N cells. In Fig. D.3, the position of the interaction point, the cone island and n-th cell are shown as the points, O, P and Q_n. At R_n, the line OQ_n intersects the plane perpendicular to OP and including P. Then the maximum radius of a cone island is defined as

$$r_{max} = \max\{PR_1, PR_2, ..., PR_n, ..., PR_N\} \qquad \text{(D.1)}$$

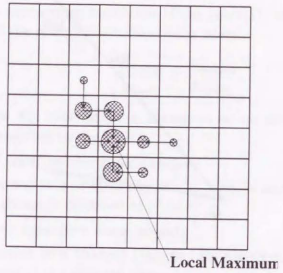

Fig. D.1: Adjacent cells are gathered around the local maxima to form 'cell islands'.

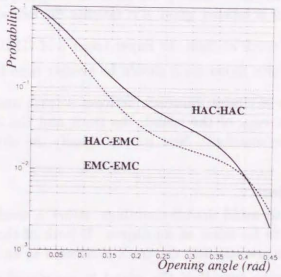

Fig. D.2: Probability functions as a function of the opening angle between cell islands.

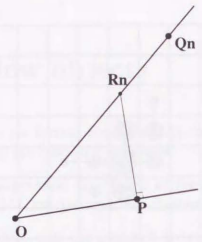

Fig. D.3: The radius of a cone island.

and it will be used for the judgement of the association with a track.

2. Only tracks with good quality are reserved for comparing with cone islands. A track is labeled 'good' if it satisfies the following conditions.
   - It should reach at least the Super Layer 3 of CTD.
   - Its transverse momentum should be greater than 0.1GeV.
3. If the distance of closest approach between a track and a cone island is shorter than r_{max} of the island, the track and the cone island are supposed to be 'matched'. Now we can classify the objects into three types.

Matched object :

In order to avoid double-countings, either a track or a cone island has to be taken as an object. If both of the following two conditions are satisfied, the track is decided to be taken.

- To make sure that the island is associated with the track alone, the following condition is required:

$$\frac{E_{island}}{p_{track}} < 0.8 + \Delta(\frac{E_{island}}{p_{track}}) \tag{D.2}$$

where $\Delta(E_{island}/p_{track})$ represents the error of the measured ratio E_{island}/p_{track}.

- The momentum resolution of the track[81] should be better than the energy resolution of the island:

$$\frac{\delta p_{track}}{p_{track}} < \frac{\delta E_{island}}{E_{island}}. \tag{D.3}$$

Otherwise the cone island is chosen to be an object. The pion mass is assigned to the object.

Cone island with no matched tracks :

It is regarded as a neutral object. Its mass is assumed be 0 and the momentum is obtained as $p^2 = E^2$.

Track with no matched cone islands :

It is regarded as a charged particle. Its energy is calculated assuming that it is a charged pion.

E. Exponential fall-off behaviour of the non-diffractive events

The $dN_{nondiff}/d\ln M_X^2$ falls off exponentially assuming the uniform and uncorrelated particle emission in rapidity y[1, 82, 83]:

$$\frac{dn_{particle}}{dy} = const. \tag{E.1}$$

Here y is taken along the beam axis in the $\gamma^* p$ system, but the axis is almost the same as the proton beam direction in the laboratory frame.

Since the center-of-mass energy of the $\gamma^* p$ system is no other than W, the y can reach to the maximum and minimum values of,

$$\begin{cases} y_{max} = \frac{1}{2}\ln\frac{W^2}{m^2+p_t^2} \\ y_{min} = -y_{max} \end{cases}. \tag{E.2}$$

Then W can be expressed with the difference of y_{max} and y_{min} as

$$W^2 = c_0 \cdot \exp(y_{max} - y_{min}) \tag{E.3}$$

where c_0 is a constant. However, W cannot be measured fully because of the limited geometrical acceptance of FCAL. Therefore, the reduced mass, which pretends to be M_X, can be reconstructed from particles detected in the detector,

$$M_X^2 = c_0 \cdot \exp(y_{limit} - y_{min}) \tag{E.4}$$

where y_{limit} corresponds to the rapidity at the inner edge of FCAL. From the equations (E.3) and (E.4), the measured M_X for the non-diffractive events can be written as

$$M_X^2 = W^2 \cdot \exp(y_{limit} - y_{max}). \tag{E.5}$$

However, the detected particle with the maximum rapidity is not necessarily emitted to y_{limit}; it would be inward of CAL in general. Suppose the gap between the maximum rapidity and y_{limit} is Δy, the equation (E.5) should be modified to

$$M_X^2 = W^2 \cdot \exp(y_{limit} - \Delta y - y_{max}). \tag{E.6}$$

Since we assume the uniform and uncorrelated rapidity distribution at (E.1), the probability that there is no particle in the gap Δy can be considered to obey Poisson statics like,

$$\frac{dP}{d(\Delta y)} = \exp(-b\Delta y) \tag{E.7}$$

where b is a constant corresponding with the density of particles in the rapidity space.

At last, combining the equations (E.6) and (E.7) leads to the exponential fall-off behaviour of non-diffractive events:

$$\frac{dN_{nondiff}}{d\ln M_X^2} = c \cdot \exp(b \cdot \ln M_X^2). \tag{E.8}$$

Note b in (E.8), which is the same as the b in (E.7), represents steepness of the exponential slope.

F. Comparison of the particle multiplicity

Fig. F.1 shows the number of CTD tracks after selecting the events with $\ln M_X^2 < 5$. In the figure, the dots and histograms are for the data and MC, respectively. Selecting the events with CTD vertex corresponds to removing the events with no tracks in CTD. As seen in Fig. F.1, the MC does not describe the data where the number of tracks is equal to 0 or 1.

As W increases, the $\gamma^* p$ center-of-mass system is boosted to the rear direction and more and more particles are emitted outside the CTD acceptance. That is the reason why the vertex finding efficiency becomes worse as W increases. However, the W dependence of the efficiency in the data is more rapid than that in the MC. It is the reason for reducing the value of $\bar{\alpha}_{I\!P}$ after the vertex requirement.

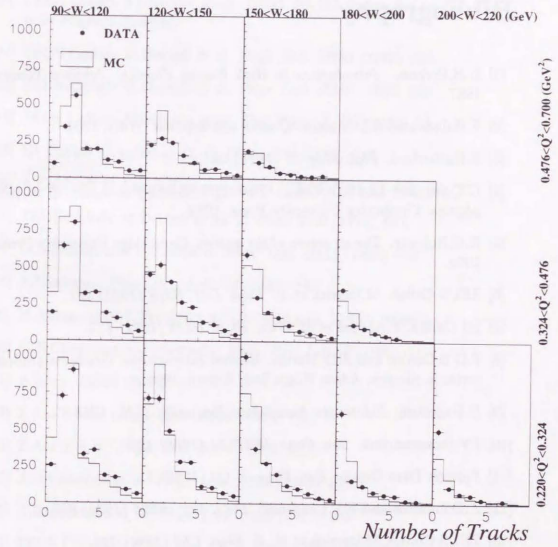

Fig. F.1: The distributions of charged track multiplicity after selecting the events with $\ln M_X^2 < 5$. The dots represent the data and the histograms are for the MC.

Bibliography

[1] D.H.Perkins. *Introduction to High Energy Physics.* Addison-Wesley, 1987.

[2] F.Halzen and A.D.Martin. *Quarks and Leptons.* Willy, 1984.

[3] E.Rutherford. *Phil. Mag. 21 (1911) 669.*

[4] G.Goldhaber and R.N.Cahn. *The experimental foundation of particle physics.* Cambridge University Press, 1988.

[5] R.G.Roberts. *The structure of the proton.* Cambridge University Press, 1990.

[6] ZEUS Collab. M.Derrick et al. *Phys. Lett. B315 (1993) 481.*

[7] H1 Collab. T.Ahmed et al. *Nucl. Phys. B429 (1994) 477.*

[8] P.D.B.Collins and A.D.Martin. *Hadron Interactions.* Graduate student series in physics, Adam Hilger Ltd, Bristol, 1984.

[9] R.Hagedorn. *Relativistic kinematics.* Benjamin, N.Y., 1963.

[10] I.Y.Pomeranchuk. *Sov. Phys. JETP 34 (1958) 499.*

[11] Particle Data Group. *Eur. Phys. J. C3 (1998) 1.*

[12] A.Donnachie and P.V.Landshoff. *Phys. Lett. B296 (1992) 227.*

[13] ZEUS Collab. M.Derrick et al. *Z. Phys. C63 (1994) 391.*

[14] H1 Collab. S.Aid et al. *Z. Phys. C69 (1995) 27.*

[15] ZEUS Collab. J.Breitweg et al. *Z. Phys. C75 (1997) 421.*

[16] H1 Collab. C.Adloff et al. *Z. Phys. C74 (1997) 221.*

[17] E.A.Kuraev L.N.Lipatov and V.S.Fdin. *Sov. Phys. JETP 44 (1976) 443.*

[18] E.A.Kuraev L.N.Lipatov and V.S.Fdin. *Sov. Phys. JETP 45 (1977) 199.*

[19] Y.Y.Balitski and L.N.Lipatov. *Sov. J. Nucl. Phys. 28 (1978) 822.*

[20] ZEUS Collab. J.Breitweg et al. *DESY 98-121 (submitted to The European Physical Journal).*

[21] ZEUS Collab. M.Derrick et al. *Phys. Lett. B356 (1995) 601.*

[22] ZEUS Collab. M.Derrick et al. *Phys. Lett. B380 (1996) 220.*

[23] ZEUS Collab. J.Breitweg et al. *Eur. Phys. J. C6 (1999) 43.*

[24] H1 Collab. C.Adloff et al. *Z. Phys. C76 (1997) 613.*

[25] A.Caldwell M.Jing S.Ritz and Q.Zhu. *ZEUS-Note 94-129.*

[26] ZEUS Collab. M.Derrick et al. *Z. Phys. C69 (1996) 607.*

[27] G.Ingelman and P.E.Schlein. *Phys. Lett. B152 (1985) 256.*

[28] J.J.Sakurai. *Phys. Rev. Lett. 22 (1969) 981.*

[29] H.Abramowicz L.Frankfurt and M.Strikman. *DESY 95-047.*

[30] G.F.Chew and S.C.Frautschi. *Phys. Rev. Lett. 8 (1962) 41.*

[31] A.Levy. *DESY 97-013.*

[32] Z.Asa'd et al. *Phys. Lett. B128 (1983) 124.*

[33] Z.Asa'd et al. *Phys. Lett. B130 (1983) 335.*

[34] A.Breakstone et al. *Phys. Lett. B132 (1983) 458.*

[35] A.Breadktone et al. *Phys. Lett. B132 (1983) 463.*

[36] ZEUS Collab. M.Derrick et al. *Z. Phys. C69 (1995) 39.*

[37] H1 Collab. S.Aid et al. *Nucl. Phys. B463 (1996) 3.*

[38] ZEUS Collab. M.Derrick et al. *Z. Phys. C73 (1997) 253.*

[39] G.Jaroszkiewicz and P.V.Landshoff. *Phys. Rev. D10 (1974) 170.*

[40] A.H.Mueller. *Phys. Rev. D2 (1979) 2963.*

[41] *The ZEUS Detector, Status Report 1993 DESY(1993).*

[42] K.Desler. *ZEUS-Note 97-084.*

[43] T.Kamon et al. *Nucl. Instr. and Meth. A213 (1983) 261.*

[44] R.Kijima. *Master's Thesis, 1995, University of Tokyo.*

[45] M.Gospic and H.Groenstege. *ZEUS-Note 96-006.*

[46] MOZART: ZEUS detector simulation program.

[47] GEANT3.13: R.Brun et al. *CERN DD/EE/84-1 (1987).*

[48] A.Kwiatkowski H.Spiesberger and J.J. Möhring. *Proceedings of the Workshop on PHysics at HERA, DESY Vol.3 (1992) 1294.*

[49] A.Kwiatkowski H.Spiesberger and J.J. Möhring. *Z.Phys. C50 (1991) 165.*

[50] M.Kasprzak. *PhD Thesis, Warsaw University, DESY F35D-96-16.*

[51] V.R.Webber. *Ann. Rev. Nucl. Part. Sci. 36 (1986) 253.*

[52] G.Marchesini et al. *Phys. Comp. Phys. Comm. 67 (1992) 465.*

[53] UA5 Collab. G.J.Alner et al. *Phys. Lett. B160 (1985) 193.*

[54] UA5 Collab. G.J.Alner et al. *Phys. Lett. B160 (1985) 199.*

[55] UA4 Collab. D.Bernard et al. *Phys. Lett. B166 (1986) 459.*

[56] R.Hagedorn. *Riv. Nouvo Cim 6 (1983) 1.*

[57] ZEUS Collab. M.Derrick et al. *Z. Phys. C67 (1995) 227.*

[58] S.Jadach. *Comp.Phys.Comm. 9 (1975) 297.*

[59] T.H.Bauer et al. *Rev. Mod. Phys. 50 (1978) 261.*

[60] F.Jacquet and A.Blondel. *DESY 79-048.*

[61] T.C.Awes et al. *Nucl. Instr. and Meth. 311 (1992) 130.*

[62] B.Surrow. *PhD Thesis, 1998, University of Hamburg.*

[63] T.Monteiro. *PhD Thesis, 1998, University of Hamburg.*

[64] U.Fricke and V.Monaco. *private communicaton.*

[65] P.de Jong. *ZEUS-Note 92-019.*

[66] S.M.Wang. *ZEUS-Note 96-121.*

[67] A.Savin. *ZEUS-Note 98-007.*

[68] ZEUS Collab. M.Derrick et al. *Z. Phys. C70 (1996) 391.*

[69] ZEUS Collab. J.Breitweg et al. *Eur. Phys. J. C1 (1998) 81.*

[70] S.Mine. *Master's Thesis, 1993, University of Tokyo.*

[71] S.Mine K.Tokushuku and S.Yamada. *Nucl. Instr. and Meth. A357 (1994) 535.*

[72] M.Nakao. *PhD Thesis, 1994, University of Tokyo.*

[73] G.D'Agostini. *DESY 94-099.*

[74] ZEUS Collab. J.Breitweg et al. *DESY 98-107 (submitted to The European Physical Journal).*

[75] J.H.Vossebeld S.Schlenstedt and F.Pelucchi. *ZEUS-Note 96-104.*

[76] M.Arneodo and M.Capua. *private communication.*

[77] H.Abramowicz E.M.Levin A.Levy and U.Maor. *Phys. Lett. B269 (1991) 465.*

[78] H.Abramowicz and A.Levy. *DESY 97-251.*

[79] M.Inuzuka. *Master's Thesis, 1996, University of Tokyo.*

[80] G.Briskin. *PhD Thesis, 1998, University of Tel Aviv.*

[81] G.F.Hartner Y.Iga J.B.Lne and N.A.McCubbin. *ZEUS-Note 96-013.*

[82] S.Jadach M.Jezabek and W.Placzek. *Phys.Lett. B248 (1990) 417.*

[83] R.P.Feynman. *Photon-Hadron Interactions.* Benjamin, N.Y., 1972.